Word Count: 9382 REVISION #3 MANUSCRIPT 7910R3

A theoretical and experimental investigation of hetero- versus homo-connectivity in barium silicates

Benjamin J. A. Moulton[a,b], Eduardo O. Gomes[c], Thiago R. Cunha[a,b], Carsten Doerenkamp[d], Lourdes Gracia[c,e], Hellmut Eckert[d,f], Juan Andrés[c], and Paulo S. Pizani[a,b]

[a]*Universidade Federal de São Carlos, Departamento de Física, Rod. Washington Luis, Km 235 13565-905 São Carlos, SP, Brazil*

[b]*CERTEV — Center for Research, Technology, and Education in Vitreous Materials, Department of Materials Engineering, Federal University of São Carlos, 13565 - 905 São Carlos-SP, Brazil: www.certev.ufscar.br*

[c] *Departament de Química Física i Analítica, Universitat Jaume I, 12071, Castelló de la Plana, Spain*

[d] *Institute of Physics in São Carlos, University of São Paulo, São Carlos, SP 13566-590, Brazil.*

[e] *Department of Physical Chemistry, University of Valencia (UV), 46100 Burjassot, Spain*

[f] *Institute of Physical Chemistry, Westfälische Wilhelms-Universität Münster, Corrensstrasse 28/30, 48149, Münster, Germany.*

Abstract

Barium silicates may be found in contact aureoles and are used in several important technologies (e.g. LEDs). The BaO-SiO_2 system stabilizes 13 crystalline phases with different silicate tetrahedral and connectivity profiles. Aside from phases composed of a single structural unit (isolated or homo-connected tetrahedra) one encounters the relatively rare case of hetero-connected tetrahedra in which varying proportions of several Q^n species are linked together. Here, we analyze the ^{29}Si MAS NMR and Raman spectroscopic manifestations of the connectivities in seven barium silicates: Ba_2SiO_4, high-$BaSiO_3$, $Ba_4Si_6O_{16}$, $Ba_5Si_8O_{21}$, $Ba_6Si_{10}O_{26}$, high-$BaSi_2O_5$ and sanbornite (low-$BaSi_2O_5$). The structures and purity of these phases were confirmed by Rietveld refinement. From the Raman spectroscopic database on 144 predominantly homo-connected crystalline silicates, the mean Q^n mode frequencies ($\nu_{Qn} \pm 1\sigma$) are found at 827.7 (±13.8) cm^{-1} for Q^0, 905.3 (±22.1) cm^{-1} for Q^1, 993.5 (±25.9) cm^{-1} for Q^2, and 1068.4 (±17.6) cm^{-1} for Q^3 units. Experimentally, homo-connected barium silicates show good agreement with these values whereas the hetero-connected phases show a wider range of ν_{Q2} than of ν_{Q3} frequencies. While the ^{29}Si NMR chemical shifts of the barium silicates are in agreement with known structural trends, those measured for the Q^2 resonances remain essentially constant, which may be caused by the lattice distortion around the large Ba^{2+} cations. To complement and rationalize experimental measurements, first-principles calculations, at the

density functional theory level, have reproduced measured frequencies within a mean absolute deviation of less than 7 cm^{-1}. Our work highlights how the results provided by ^{29}Si NMR and Raman spectroscopies, and *ab initio* calculations can be combined to rationalize the structure of complex systems. Present findings also shed light on the vibrational modes that may be used to track bond lengths *in situ* at extreme conditions and the behavior of homo- versus hetero-connectivity, revealing clear implications for evaluating silicate glasses and melts where hetero-connectivity is the rule rather than the exception.

Keywords: Barium silicates, Ba_2SiO_4, high-$BaSiO_3$, $Ba_4Si_6O_{16}$, high-$Ba_5Si_8O_{21}$, $Ba_6Si_{10}O_{26}$, high-$BaSi_2O_5$ and low-$BaSi_2O_5$, ^{29}Si MAS NMR and Raman spectroscopies, X-ray diffraction, density functional theory calculations.

1 Introduction

During the last decade, the study of barium silicates represents an exceptional part in a wide field of crystallographic and material science because of their applications in different fields. For example, barium silicate-based ceramics are used as solid-oxide sealant materials (e.g. Namwong et al. 2010), erasable-writable optical storage devices (Lin et al. 2019), and, when doped with rare-earth elements, as light emitting diode materials (Xiao et al. 2009; Chen et al. 2015). Barium silicates are built of SiO_4^{n-} tetrahedra, the fundamental building blocks of almost all silicate minerals and liquids (Liebau 1985). Its remarkable stability through the transition from the solid into the liquid state is central to understanding and predicting the properties of silicate crystals, glasses, and melts. The modified random network model of silicate liquids describes them as having two entangled subnetworks: one constructed from interconnected silica tetrahedra and one comprised of ill-defined modifier-oxygen polyhedra (MO_x, where M = K, Ba, etc.) (c.f. Greaves 1985). The silica subnetwork contains tetrahedra that may be connected by up to four additional tetrahedra units. Connectivity is defined by the number of Si-O-Si bonds found around a central tetrahedron and described using the Q^n species notation, where *n* is the number of bridging oxygen (BO) atoms shared between tetrahedra and 4-*n* is the number of non-bridging oxygen (NBO) atoms bound to M cations (c.f. Calas et al. 2006). Most crystalline silicates are

63 built from a single Q^n species, whereas in silicate liquids and glasses have two or more Q^n
64 species that are assumed to be randomly linked. Sanbornite, low-$BaSi_2O_5$, is an uncommon
65 mineral composed of Q^3 units and can be found in the metamorphic aureole associated with a
66 migmatite and granodiorite pluton at Big Creek, California, USA (Douglass 1958; Walstrom and
67 Leising 2005).

68 Barium silicates stabilize a wide range of structures from neso- (Q^0), ino- (Q^2), and phyllo-
69 (Q^3) silicates including Ba_2SiO_4, $BaSiO_3$, and $BaSi_2O_5$ which are built from a single Q^n species
70 (Eskola 1922; Roth and Levin 1959; Oehlschlegel 1975; Shukla et al. 2018). When bonding is
71 between Q^n of equal *n*, e.g. Q^3-Q^3, we refer to this as *homo-connectivity*. Also present are
72 $Ba_4Si_6O_{16}$, $Ba_5Si_8O_{21}$, and $Ba_6Si_{10}O_{26}$ which are uncommon non-hydrous crystal structures built
73 from both Q^2 and Q^3 species, which are also interconnected (Liebau 1985). In this
74 mineralogically rare situation, where Q^n are bound to $Q^{n\pm1}$, e.g. Q^2-Q^3 linkages, we refer to this
75 as *hetero-connectivity* (Fig. 1). By far the most common hetero-connective mineral phases are
76 found within the amphibole group (e.g. tremolite, $Ca_2Mg_5Si_8O_{22}(OH)_2$), which have complex
77 chemistry including hydroxyl groups. The three hetero-connective phases, $Ba_6Si_{10}O_{26}$, $Ba_5Si_8O_{21}$,
78 and $Ba_4Si_6O_{16}$, have Q^2:Q^3 ratios that increase with increasing Ba content from 1:4 to 1:3 to 1:2,
79 respectively (Table 1). Beyond their structures (Hesse and Liebau 1980a) and thermal expansion
80 behavior (Gorelova et al. 2016), little is known about these hetero-connected phases. In contrast,
81 the structure and properties of the homo-connected phases Ba_2SiO_4 (Q^0), high-$BaSiO_3$ (Q^2), and
82 the two Q^3 polymorphs, sanbornite (orthorhombic low-$BaSi_2O_5$) and monoclinic high-$BaSi_2O_5$,
83 have been the focus of many studies using X-ray diffraction (Grosse and Tillmanns 1974a,
84 1974b; Hesse and Liebau 1980a, 1980b; Cormier et al. 1999; Schlenz et al. 2002; Denault et al.
85 2015; Gorelova et al. 2016), nuclear magnetic resonance (NMR) (^{29}Si: Smith et al., (1983), ^{17}O:
86 Thompson et al., (2012)), Raman (Takahashi et al. 2010; Moulton et al. 2019), Si *K*-edge and Ba
87 L_3-edge XANES, X-ray photoemission (XPS) (Bender et al., 2002;), and atomic force
88 microscopy (Schlenz et al. 2002).

89 Advances of experimental characterization techniques, especially solid-state NMR and
90 Raman spectroscopy, and first-principles calculations have significantly improved the
91 understanding of the structures of these systems. This study expands upon our recent analysis of
92 the vibrational modes of sanbornite and $Ba_5Si_8O_{21}$ (Gomes et al. 2021) and here we investigate

the effects of SiO_4 connectivity on the spectroscopic signature of the Q^n units in Ba_2SiO_4, high-$BaSiO_3$, $Ba_4Si_6O_{16}$, $Ba_5Si_8O_{21}$, $Ba_6Si_{10}O_{26}$, high-$BaSi_2O_5$ and sanbornite (low-$BaSi_2O_5$). As a first step, the crystal lattice parameters were determined using Rietveld refinement of powder diffraction and first-principles calculations. Second, the ^{29}Si magic spinning angle nuclear magnetic resonance (MAS NMR) and Raman spectra were used to identify features associated with each of the contributions of the Q^n species within these structures. Finally, an evaluation of the vibrational modes and their origin is reported based on simulation results using *ab initio* calculations at the density functional level of theory (e.g. Gomes et al. 2019). The theoretical and experimental results are in excellent agreement and clearly reveal the differences between homo- and hetero-connectivity in barium silicates. We conclude by emphasizing some of the implications for the interpretation of Raman spectra of silicate liquids and glasses (e.g. Moulton et al. 2018), where hetero-connectivity is the rule rather than the exception.

Ba_2SiO_4 is composed of isolated tetrahedra (Q^0 species) surrounded by Ba^{2+} cations which form an arcanite-type (β-K_2SO_4) structure (McGinnety 1972). The composition range $BaSiO_3$-$BaSi_2O_5$, including the hetero-connective phases, form a series with the general formula $Ba_{m+1}Si_{2m}O_{5m+1}$. Here m = 1, 3, 4, 5, or ∞, and is the number of silica tetrahedra which form the *zweier* single chains, m = 1, ribbons or *zweier* triple–quintuple chains, for m = 3-5, and ultimately, sheets, for m = ∞ (Fig. 1); e.g. sanbornite (Hesse and Liebau 1980a, 1980b). Ba^{2+} is able to stabilize these structures due to its low electronegativity, 0.89, and large ionic radius, 1.35 Å (Brown and Altermatt 1985; Gagné and Hawthorne 2015). As a result, barium silicates can be formed with a wide range of topologies. In fact, Liebau (1985) noted that the Ba- and Si-substructures stretch and twist so that the diameter of one BaO_x polyhedron is approximately equal to Si-Si distance. This produces an internal strain on these tetrahedra making these chains quite stretched compared to other, smaller alkaline-earth-bearing inosilicates. This is the explanation of why no Q^1 phase, e.g. $Ba_3Si_4O_{11}$, is known, because the extreme strain is more than can be accommodated by stretching or twisting adjacent tetrahedra (Liebau 1985). The topologies of the barium silicates and how they compare to other silicate groups are further discussed in recent articles (Hawthorne et al. 2019; Day and Hawthorne 2020).

This is the peer-reviewed, final accepted version for American Mineralogist, published by the Mineralogical Society of America.
The published version is subject to change. Cite as Authors (Year) Title. American Mineralogist, in press.
DOI: https://doi.org/10.2138/am-2021-7910. http://www.minsocam.org/

2 Experimental and theoretical procedures

2.1 Synthesis of barium silicate powders

Batches of 3-5 g of high-purity SiO_2 and $BaCO_3$ (Sigma-Aldrich, >99.9%) reagents where used to synthesize the crystalline xBaO·(1-x)SiO_2 (x = 0.33, 0.375, 0.385, 0.40, 0.50, and 0.66) phases. The solid-state reaction procedure of Gorelova et al., (2016) was followed where between successive heat treatments the samples were repeatedly ground and pressed into tablets. Heat treatment protocols comprised two steps prior to the final temperature: a low-temperature heating step (1 h at 500°C) for removing polyvinyl butyral (used as a binder material to increase the density) of the pellets, followed by calcination for 1 h at 1000°C. The crystalline samples where ground using a mixture of sample plus ZrO_2 balls in a high-energy vibrating mill for 2 h. The milled powders produce very-fine and evenly distributed grain sizes resulting in an improved compositional homogeneity. This is critical to reduce the number of phases present in this system where the compositions of stable phases differ by only a few mole percent.

2.2 Characterization of the samples

All the crystal structures have been confirmed using X-ray diffraction (XRD). XRD measurements were made on a Rigaku Ultima IV machine using Cu K_α radiation operating at 40 kV and a current of 20 mA using continuous scanning mode (0.5° min^{-1}) with a 2θ step of 0.02° between $10° \leq 2\theta \leq 80°$. The diffraction patterns were refined using the GSAS program (Rietveld 1967; Larson and Von Dreele 2004) and show that the crystalline phases are of high purity and contain <1% of any impurity.

The Raman spectra were taken on a LabRAM HR800 spectrometer using a 532 nm wavelength laser which supplied ~20 mW on the sample. Spectra were taken using a 100X visible objective (lateral spatial resolution ~1 μm), 100 μm pinhole, and an 1800 gr/mm grating between 10 – 1600 cm^{-1} or greater range (resolution ≤0.5 cm^{-1}). Raman spectra of the crystalline phases were measured using 12 accumulations and a dwell time of 5 s. Reported spectra below are normalized to the intensity of the most intense band, representing the symmetric stretching mode. In order to characterize the vibrational modes, the spectra first had a flat baseline removed, except near the laser line, and were then curve fit using Lorentzian lineshapes to determine the mode character. This procedure yielded excellent fits to the spectra overall.

This is the peer-reviewed, final accepted version for American Mineralogist, published by the Mineralogical Society of America.
The published version is subject to change. Cite as Authors (Year) Title. American Mineralogist, in press.
DOI: https://doi.org/10.2138/am-2021-7910. http://www.minsocam.org/

The solid-state ^{29}Si MAS NMR spectra were recorded with an Agilent DD2 spectrometer operating at 5.64 T. The measurements were conducted in a 7.5 mm MAS-NMR probe, using π/2 pulses of 5.5 µs length, a rotation frequency of 5.0 kHz and a relaxation delay of up to 30 000 s, depending on relaxation characteristics, ensuring quantitatively reliable detection. The chemical shifts are reported relative to tetramethylsilane using $CaSiO_3$ as a secondary reference (δ = –71.33 ppm). All line shape deconvolutions were done using the DMFIT software (Massiot et al. 2002).

2.3 Computational methods and model systems

Density functional theory (DFT) level calculations of the lattice parameters and vibrational modes were carried out using Becke's three-parameter hybrid non-local exchange functional, combined with a Lee-Yang-Parr gradient-corrected correlation functional (B3LYP), implemented in the CRYSTAL17 package (Dovesi et al. 2018). The centered atoms were described using pseudopotential databases: (Towler 1996), 88-31G* (Nada et al. 1996) and 8-411d11G (Valenzano et al. 2006) (all-electron) for Ba, Si and O, respectively. In relation to the diagonalization of the density matrix, the reciprocal space net was described using a shrinking factor of 4 and generated according to the Monkhorst–Pack scheme. The accuracy of the evaluation of the Coulomb and exchange series was controlled by five thresholds at values of 10^{-7}, 10^{-7}, 10−7, 10^{-7}, and 10^{-14}. The vibrational frequencies calculation was performed at the Γ point within the harmonic approximation, and the dynamic matrix was computed by the numerical evaluation of the first derivative of analytical atomic gradients. The optimized structural parameters of the crystal structures are reported in Table 1. We have used the same procedure here as in our initial works, first on $BaMoO_3$ (Gomes et al. 2019) and more recently on sanbornite and $Ba_5Si_8O_{21}$ (Gomes et al. 2021).

3 Results

The results of the bulk structural analysis from experimental measurements and first principle calculations are reported before discussing the Raman and ^{29}Si MAS NMR spectra. For simplicity the phases are referred to by their $BaO:SiO_2$ molar ratios, as indicated in the ID of Table 1. For example, monoclinic $Ba_4Si_6O_{16}$ is denoted **B4S6**.

This is the peer-reviewed, final accepted version for American Mineralogist, published by the Mineralogical Society of America.
The published version is subject to change. Cite as Authors (Year) Title. American Mineralogist, in press.
DOI: https://doi.org/10.2138/am-2021-7910. http://www.minsocam.org/

3.1 Crystal structures determined by XRD

The crystal cell dimensions, β angles and volumes are reported in Table 1. An example of the Rietveld refinement of B6S10 is provided in Figure 2. Individual refinements are shown in the supplementary material, Section S2 (Fig. S1). The cell volumes of the barium silicates derived from Rietveld refinements are within <1% of reported values (Grosse and Tillmanns 1974b, 1974a; Hesse and Liebau 1980a, 1980b). The relaxed cell volumes of the DFT simulations reproduce the reported values within <4%. Therefore, the experimental and calculated crystal structures are in good agreement.

3.2 ^{29}Si NMR results

Single sharp peaks are observed at -93.1 ppm for low-BS2, -80.0 ppm for high-BS, and -70.1 ppm for B2S (Fig. 3), in agreement with published values (Smith et al. 1983; Mägi et al. 1984; Murdoch et al. 1985). The hetero-connected barium silicates show a range of chemical shift values consistent with those expected for other Q^2- and Q^3-bearing phases (Table 2). In samples containing multiple Si sites, the relative peak areas are in excellent agreement with the expected proportions. The NMR spectra of the hetero-connected B4S6, B5S8, and B6S10 phases are reported here for the first time.

3.3 Raman spectra and their vibrational mode assignments

The Raman spectra of the barium silicates are dominated by intense peaks in the 400-800 cm^{-1} (Fig. 4a) and 800-1200 cm^{-1} (Fig. 4b) ranges that correspond to the *bending* and *stretching* mode regions, respectively (c.f. Gomes et al. 2021). Table 3 summarizes the observed high-intensity Raman peaks. A detailed discussion of all modes is beyond the focus of this work; however, a full analysis of all vibrational modes is provided in supplementary material Sections S3 and S4. In Table 4 a complete mode analysis of Ba_2SiO_4 is provided as an example. Given the numerous vibrational modes (e.g. Table S3) and the small frequency differences among them, further refinement of our interpretation through polarized or oriented single crystal investigations should be possible. Given the complexity of the Raman spectra (Fig. S2), we emphasize that the overall agreement between theoretical and experimental values is excellent.

An analysis of the results for high-BS renders that the intense band at 599.8 cm^{-1} is associated with Si-O1-Si bending motion (Table S2). The symmetry of high-BS, $P2_12_12_1$, is unique among the phases studied and the 599.8 cm^{-1} band is displaced from those belonging to

the bending modes of the other phases. The intense bands originating from the bending modes of the B4S6-BS2 phases display a doublet or triplet feature centered around ~530 cm^{-1} (Fig. 4a). B4S6, B5S8, B6S10 and high-BS2 have similar unit cell symmetries, either $P2_1/c$ or C2/c, and similar intense bending mode frequencies. Despite the observed similarities in the spectra, the origins of these modes are quite distinct. For example, in low-BS2 the 535.5 cm^{-1} mode involves bending of the O3-Si-O2, where one oxygen is a BO and the other a NBO (Table S7). In contrast, the 533.8 cm^{-1} mode of high-BS2 involves the bending of the Si3-O2-Ba2 bond angle (Table S6). As the origin of the intense bending modes is structure dependent, any generalizations regarding relationships between mode frequency and crystal chemical properties, such as the mean inter-tetrahedral angle, should be treated with caution, except in cases where the mode originates in the actual bending of Si-O-Si bond angles.

The higher frequency region (>800 cm^{-1}) consists of Si-O stretching modes that are often attributed to Q^n species (Fig 4b). In early studies which applied the central force model to Q^n species generated symmetric (υ_1-type) and antisymmetric (υ_3-type) stretching modes, any deviation from tetrahedral symmetry was thought to produce vibrational coupling between these modes (c.f. McMillan 1984). Vibrational coupling of υ_1- and υ_3-type modes was expected to produce frequency shifts and changes in the relative intensities of the peaks particularly in nesosilicates (Piriou and McMillan 1983). Lam et al., (1990) challenged these inferences using lattice dynamic calculations to reproduce the trends in the stretching modes of forsterite. However, as Dowty (1987) emphasizes, the term *mode coupling* has been inconsistently applied. Furthermore, the success of central force calculations in reproducing the mode frequencies has been lessened by the model dependence of these calculations. More recent DFT-based approaches (e.g. Zicovich-Wilson et al. 2004; Aliatis et al. 2015; Stangarone et al. 2017; Gomes et al. 2019, 2021) have found excellent agreement between experimental and simulated spectra without such model dependence. The results herein overwhelmingly confirm that most of the high-frequency peaks originate from specific and singular Si-O stretching vibrations regardless of the structural type or unit.

In the high-frequency region, the most intense peaks correspond to Si-O stretching modes are characteristic of the Q^n species (e.g. McMillan 1984; Nesbitt et al. 2017a, 2018, 2020). The barium silicate structures contain Q^0, as well as homo-connected Q^2 and Q^3 species, show

This is the peer-reviewed, final accepted version for American Mineralogist, published by the Mineralogical Society of America.
The published version is subject to change. Cite as Authors (Year) Title. American Mineralogist, in press.
DOI: https://doi.org/10.2138/am-2021-7910. http://www.minsocam.org/

239 stretching modes that shift from 823.8 cm^{-1} in B2S to 963.9 cm^{-1} for high-BS to 1077.7 cm^{-1} for
240 low-BS2 (Fig. 4b). The 964 cm^{-1} peak of high-BS originates from symmetric stretching motions
241 of the O3 and O2 sites away from the central Si. In contrast, the 823.7 cm^{-1} peak of B2S and the
242 1077.9 cm^{-1} peak of low-BS2 both involve the elongation of the Si-O1 bonds in their respective
243 structures. The hetero-connected phases show intense peaks around ~1065 cm^{-1} that shift to
244 higher frequencies with increasing proportion of Q^3 species. The intense high-frequency peaks of
245 B6S10, B5S8 and B4S6 are found at 1069.2, 1066.8 and 1061.0 cm^{-1}, respectively. Simulations
246 of the stretching modes lead us to conclude that the B4S6 mode at 1061.0 cm^{-1} originates from
247 Si3-O8 bond stretching (Table S3) whereas the B5S8 mode at 1066.8 cm^{-1} comes from Si3-O7
248 bond stretching (Table S4). Both of these belong to Q^3 sites which are bonded to Q^3 only.
249 Consequently, the Q^3 units do not need to be directly bonded to the Q^2 site to induce a frequency
250 shift. This indicates that the electron density is spread across the tetrahedral ribbon.

251 These hetero-connected phases display two other features that are characteristic of their
252 spectra. First, the main peaks overlap strongly with adjacent peaks, and, second, they display
253 other peak(s) centered near 925 cm^{-1} (Fig. 4b). The former feature may be expected as the
254 hetero-connected phases have three or more Si sites and many O sites. Peaks at comparable
255 wavenumbers (928.1, 924.0 and 921.3 cm^{-1}) are observed for B6S10, B5S8 and B4S6,
256 respectively, i.e., at slightly lower wavenumbers than the 963.9 cm^{-1} peak of high-BS. Again,
257 simulations lead us to conclude that the B4S6 mode, at 928.1cm^{-1}, originates from Si1-O2
258 stretching (Table S3) whereas the B5S8 mode, at 924.0 cm^{-1}, involves simultaneous stretching of
259 the Si1 away from both the O1 and O2 sites (Table S4). The trend here is that as the proportion
260 of Q^2 increases, the vibrational frequency of the Q^2 unit increases. This is the same as for the Q^3
261 units whose frequencies also increase with increasing proportion of Q^3. In both cases, the shift is
262 toward the frequency observed in the homo-connected structures.

263 The above findings correspond to the high intensity Raman modes that are obvious in the
264 spectra, however, other vibrational modes may provide insights in future studies. Full analysis of
265 the vibrational modes in the complete spectra for B2S is reported in Table 4 whereas the
266 remaining mode analysis of high-BS, B4S6, B5S8, B6S10, high-BS2, and low-BS2 are presented
267 in Table S2, Table S3, Table S4, Table S5, Table S6 and Table S7, respectively. Calculated
268 values reproduce the mode frequencies of the measured spectra with a mean absolute deviation

of <7 cm^{-1}. However, the experimental Raman spectra usually reveal only two thirds the number of expected normal modes, and consequently, there is always some ambiguity even in polarized single crystal studies (e.g. Chopelas 1991). We hope that reporting the complete mode analysis will provide insights in future studies (e.g. in studying the effects of dopants or *in situ* reactions).

4 Discussion

4.1 NMR chemical shifts and structural attributes

The most successful empirical model of the ^{29}Si NMR chemical shifts comes from Sherriff and Grundy (1988). The predictive capacity of this model is very good with $\delta_{measured}$-$\delta_{predicted}$ <2 ppm for a wide range of silicates and aluminosilicates. The isotropic chemical shift (δ) is predicted from:

$$\delta = 650.08\chi'' - 56.06 \quad (1)$$

where

$$\chi'' = \sum s((1 - 3\cos^2\theta)/3R^3)\left(\frac{\cos\alpha}{\cos\alpha - 1}\right) \quad (2)$$

Here s is the bond valence of the M-O bond, R is half the distance between the O and the second neighbour (M), and θ and α are the Si-O-M and O-M-Si angles, respectively (Sherriff and Grundy 1988). The summation includes all the second-nearest neighbors. In the present case the measured shifts are not well reproduced when all the second neighbours are included, possibly due to the high coordination number of Ba^{2+} cations. Therefore, we have tested two different constraints in calculating χ'': (i) using a cut-off distance of 3.7 Å for second neighbours (or 3.8 Å when an additional neighbour was found at the limit) or (ii) considering only the two closest second next nearest neighbours (2 NNN). Both constraints result in fewer second neighbour Ba cations being included in the calculation of χ'', and both reproduce many of the chemical shifts reasonably well, while they fail for others (see Table 5). We also find that the second constraint produces worse predictive accuracy for low-silica compositions. Overall, our results indicate that even under these constraints, χ'' does not correctly account for the influence of Ba-O bonding on the ^{29}Si chemical shifts.

The reason for the success of the Sherriff and Grundy model is that it incorporates many of the crystal chemical parameters which had already been empirically shown to have a strong

297 influence on the chemical shift, for example, the connectivity (Lippmaa et al., 1980; Smith et al.,
298 1983), the Si-O bond length (Grimmer and Radeglia, 1984), the bond strength (Mägi et al.,
299 1984), the mean inter-tetrahedral angle (Dupree and Pettifer, 1984), the electronegativity (Janes
300 and Oldfield, 1985), and the σ orbital hybridization (Engelhardt and Radeglia, 1984). Despite
301 this success, there were hints that covalency effects of non-silica second neighbours were not
302 well incorporated. For instance, Si-poor phases, e.g., nesosilicates, are somewhat less well
303 described by this model than more siliceous ones. In the original report the calculation for
304 forsterite yields a chemical shift of -67.8 ppm whereas it is measured at -62.0 ppm, which is a
305 two-to-three times worse agreement than observed for the majority of the silicates studied. More
306 recently, *ab initio* methods have been more successful at predicting the chemical shifts of
307 Mg_2SiO_4 polymorphs (e.g. Ashbrook et al. 2007), although no additional insight regarding the
308 chemical shielding of the silicate tetrahedra was offered beyond the original empirical trends.
309 Given the constraints discussed above, the experimental chemical shifts are in good agreement
310 with those predicted by the Sherriff and Grundy model (**SG88**), with $\delta_{measured}$-$\delta_{predicted}$ values
311 usually <5 ppm but as large as 12 ppm in B2S (Table 5) without any indication of systematic
312 discrepancies.

313 Although several factors affect the chemical shift, strong linear correlations with the inter-
314 tetrahedral angle have been found for three Q^3-bearing alkali phyllosilicates (De Jong et al.
315 1998), however, for barium silicates the correlation between chemical shift and inter-tetrahedral
316 angle is clearly nonlinear (Fig. 5). For hetero-connective structures, the Q^3 chemical shift appears
317 to be more sensitive to smaller inter-tetrahedral angles (<140˚) than to large ones (Table 6). In
318 contrast, the Q^2 chemical shifts considered here are almost independent of inter-tetrahedral angle.
319 Ultimately, there is an influence of mean inter-tetrahedral angle on the chemical shift, but other
320 factors need to be taken into consideration, e.g., steric limits, as the linear regressions of figure 4
321 are weak (R^2 = ~0.7).

322 The extreme shifts displayed by the barium silicate Q^2 species are more evident when the
323 overall trends between the Q^n units and chemical shift are shown (Fig. 6). This data is compiled
324 from the literature (see supplemental materials; Smith et al. 1983; Mägi et al. 1984; Kinsey et al.
325 1985; Murdoch et al. 1985; Sherriff and Grundy 1988; De Jong et al. 1998; Ashbrook et al.
326 2007). For the barium silicates which have highly strained Q^2 sites, their chemical shift is

essentially at the extreme positive end, near -80 ppm, of the distribution of literature values. The remaining Q^0 and Q^3 peaks of the barium silicates are situated near the grand mean chemical shift defined by the range of literature values for these Q^n species. Although the above discussion takes the perspective of the Q^n species above, we would point out that broadly the Q^n species correspond to crystal groups within the structural hierarchy hypothesis (Hawthorne et al. 2019): cluster silicates (Q^{0-1}), chain-ribbon silicates (Q^{2-3}), sheet silicates (Q^3) and framework silicates (Q^4).

4.2 Si-O stretching frequency versus connectivity

The stretching vibrations of the barium silicates have been plotted alongside our analysis of values taken from the RRUFF database (Lafuente et al. 2015) and published studies on the *nesosilicates* (Q^0 – Handke and Urban 1982; Piriou and McMillan 1983; Chopelas 1991; Mohanan et al. 1993; Voronko et al. 2006; Bispo et al. 2017), the *sorosilicates* (Q^1 - Tarte et al. 1973; Gabelica-Robert and Tarte 1979, 1981; Nesbitt et al. 2018), the *inosilicates* (Brawer and White 1975; Konijnendijk and Stevels 1976; Richet et al. 1998; Huang et al. 2000; Tribaudino et al. 2012, 2019; Mantovani et al. 2015; Nesbitt et al. 2018) and the *phyllosilicates* (Q^3 –Brawer and White 1975; Konijnendijk and Stevels 1976; McKeown and Bell 1998; Moulton et al. 2019) in Figure 7. The stretching modes of the phases in figure 7 were established either, because prior mode analysis has been reported, or, the modes were identified due to their intensity – usually ~10 times stronger than adjacent bands in spectra. Although clear trends are found, this was not a trivial task as the stretching modes often give rise to less intense Raman bands than the bending modes for both the phyllosilicates (e.g. Wang et al. 2015) and double chain amphiboles (e.g. tremolite-actinolite group – Apopei and Buzgar 2010; Ott and Williams 2020). These values should be taken with caution because they are only a subset within the diversity of modes in these spectra.

As with ^{29}Si chemical shifts, the extreme values for the Si-O stretching frequencies of the Q^n species somewhat overlap. For example, the ranges of stretching frequencies assigned to Q^2 and Q^3 units overlap in the 1010-1035 cm^{-1} region (Fig. 7). This region usually corresponds to differences in composition and crystal symmetry. For example, Handke and Urban, (1982) report the alkaline earth orthosilicate series, Be_2SiO_4-Ba_2SiO_4, where all intense stretching modes range from 810 to 840 cm^{-1} except for beryllium-nesosilicate which has a value of 880 cm^{-1}, closer to

the typical Q^1 frequency. The reason for this is that Be^{2+} cation is much smaller and more strongly electronegative than the other alkaline earth elements and consequently it crystallizes in the hexagonal phenakite-type structure, rather than other olivine group minerals with larger and more electropositive cations Mg^{2+} to Ba^{2+} which crystallize to orthorhombic or monoclinic structures at ambient conditions.

144 Raman spectra give a grand mean ν_{Qn} ($\pm\sigma$) frequency of 827.7 ($\pm$13.8) cm^{-1} for Q^0, 905.3 ($\pm$22.1) cm^{-1} for Q^1, 993.5 ($\pm$25.9) cm^{-1} for Q^2, and 1068.4 ($\pm$17.6) cm^{-1} for Q^3 (Fig. 7). For the homo-connected barium silicates, the main stretching frequencies are well within their respective Q^n ranges, although the Q^2 mode of BS is near the lower end of the range of Q^2 frequencies. This is consistent with above NMR results, where the Q^2 units also resonate towards the extreme end of the Q^2 chemical shifts. Above it was shown that the intense high-frequency peaks are usually related to individual Si-O stretching motions. Therefore, it is somewhat surprising that the trends in the high-intensity stretching modes are so distinct. Nonetheless, the trend is evidently robust (Fig. 7). The effects of crystal symmetry within each of the Q^n species structural groups deserves further consideration. Although the high-frequency modes originate from different bonds, the relative bond strength of the tetrahedron, related to the number of next-nearest-neighbour Si, or other tetrahedral elements, controls the values of the vibrational frequency.

4.2.1 The effect of hetero-connectivity on the stretching mode frequencies

Raman spectra of the anhydrous hetero-connected siliceous phases are rare. The series from B4S6 to B6S10 which form triple-, quadruple- and quintuple-chains containing Q^2:Q^3 ratios from 1:2 to 1:4 (Fig. 1). This series represents a rare opportunity to compare the vibrational spectra of these phases of relatively simple (e.g., anhydrous, low symmetry) and comparable chemistry (e.g. only containing Ba, Si, and O). As a result, the main structural differences associated with the localized Si-O stretching modes are related to their local bonding environments. The DFT-based simulations allow us to unveil the origin of the vibrational modes (e.g., Table 4). An analysis of these results renders that the hetero-connected phase s have a second moderately intense band near 925 cm^{-1}, which is related to the Q^2 site and another peak near 1070 cm^{-1} related to the Q^3 site (Fig. 4B). The observed shift of the former feature from 921.3 in B6S10 to 928.1 cm^{-1} in B4S6, is likewise observed in the Q^3 modes which shift from

1061 to 1069 cm^{-1}, respectively. In both the Q^2 and Q^3 cases, the shift reflects a trend towards the frequencies of the homo-connected Q^n species. It is also important to note that the relative intensity of the Q^2 peak compared to that of the Q^3 peak does not increase with increasing Q^2 content. Nonetheless, we may conclude that for barium silicates the Q^2 and Q^3 modes shift systematically to higher frequencies with increasing proportion of their respective Q^n contents. However, this also depends on how distorted these Q^n species are to begin with as Q^2 is already at the extreme end of the range of Q^2–related Si-O-Si bond angles. Next, we test these trends as compared to other hetero-connected phases, tremolite and xonotlite.

4.3 Comparison to other hetero-connected phases: Tremolite & Xonotlite

To reinforce the finding above, we compare the results on two phases that have similar chemistry, 'simple' alkaline-earth-bearing silicates, by analyzing available structural and spectroscopic data. The first mineral considered is the amphibole endmember tremolite, $Ca_2Mg_5Si_8O_{22}(OH)_2$, which has two tetrahedral sites, one Q^2 and one Q^3 in equal proportion. The second mineral is xonotlite ($Ca_6Si_6O_{17}(OH)_2$), which has a Q^2:Q^3 ratio of 2:1. Tremolite contains a double chain where *every other* tetrahedron is a Q^3 unit which links the two chains forming six-membered rings (Hawthorne and Grundy 1976; Gibbs et al. 2005; Antao et al. 2008). Xonotlite also has double chains but with *every third* tetrahedron is crosslinked by a Q^3 site (Brown 1978; Kudoh and Takéuchi 1979; Hejny and Armbruster 2001). Their Raman and ^{29}Si MAS NMR spectra have been reported (Mägi et al., 1984; Apopei and Buzgar, 2010; Frost et al., 2012) and their stretching mode positions have been included in figures 6 and 7.

In terms of ^{29}Si MAS NMR, both xonotlite and tremolite show Q^2 chemical shifts near the average value observed for crystalline compounds containing Q^2 species, at -87 ppm (Fig. 6). The chemical shift of the Q^3 species in xonotlite adopts a near-extreme value at -97.6 ppm whereas in tremolite this peak is found at -92.2 ppm. Xonotlite shows a Q^2-Q^3 peak separation of 11 ppm, comparable to the separation observed in the hetero-connected barium silicates whereas the separation is only ~5 ppm for tremolite (Table 5). Tremolite, containing the smaller Mg cation, does not appear to show a large distortion of the tetrahedral ribbons whereas the Ca-rich xonotlite is considerably distorted and shows a large separation between Q^2 and Q^3 peaks. Apparently, the influence of the hydroxyl groups on the chemical shielding is smaller than the distortion produced simply from having large counterions like Ca^{2+} or Ba^{2+} cations. This

comparison suggests that the Q^3 site of xonotlite is considerably strained whereas it is the Q^2 sites in the hetero-connected barium silicates, which appears to be strained (e.g. note the tetrahedra volumes in Table 6).

In terms of Raman spectra, xonotlite and tremolite show similar behavior as B4S6, B5S8 and B6S10 (Fig. 7). The wavenumbers observed for the Q^2 unit of xonotlite (962.5 cm^{-1}) and BS are essentially equal whereas that of the Q^3 band is found to be slightly lower (1044 cm^{-1}) than those in the barium-containing phases (~1070 cm^{-1}). In view of the previously discussed trends this shift is expected given that there are more Q^2 than Q^3 units in the xonotlite structure. In contrast, the intense Raman bands of Q^2, at 929 cm^{-1}, and the Q^3 mode, at 1059 cm^{-1}, of tremolite appear at very similar frequencies as those observed in the hetero-connected barium phases. This is expected as tremolite has equal proportions of Q^2 and Q^3 units and thus can be considered structurally similar to the B4S6 phase.

In summary, the general trends found among anhydrous barium silicates are consistent with other hetero-connective phases with some subtle differences related to the distortion among sites within each structure. This comparison shows a more systematic behavior of Raman modes in hetero-connected phases whereas the relationship between ^{29}Si chemical shifts and local geometry appears to be more complex. Understanding the subtleties highlighted here will hopefully lead us to a better understanding of why the clear trends in NMR peaks of the alkali silicate glasses are better reproduced than those of alkaline earth silicates glasses (e.g. Pedone et al. 2010; Charpentier et al. 2013).

4.4 On the complementary nature of NMR and Raman measurements

The above results of barium silicates point out important differences between the Q^n group signatures in NMR and Raman spectroscopy. The inferences of one are not directly applicable to the other, nor vice versa. In fact, while the correlations between vibrational wavenumber or chemical shifts with the type of structural group have a well-established positive correlation (Fig. 6,7), structural trends *within a Q^n group* are essentially orthogonal (dashed lines in Fig. 8) to the general trend. For example, in the present barium silicates the ^{29}Si chemical shifts of the Q^3 units show a broad distribution across ~10 ppm whereas the Q^2 peaks shift over a much narrower range, only ~2 ppm. In contrast, the Raman mode wavenumbers display the opposite behavior. For the Q^2 stretching modes, variations on the order of ~40 cm^{-1} are observed whereas the Q^3

This is the peer-reviewed, final accepted version for American Mineralogist, published by the Mineralogical Society of America.
The published version is subject to change. Cite as Authors (Year) Title. American Mineralogist, in press.
DOI: https://doi.org/10.2138/am-2021-7910. http://www.minsocam.org/

modes only spread across half this range, ~20 cm^{-1}. These differences arise because the Q^n chemical shifts are strongly influenced by the second nearest neighbours, whereas the vibrational modes associated with the Q^n units are highly localized, often to specific Si-O bonds. As a result of this behavior, the main bands in the Raman spectra do shift systematically in frequency, even in the hetero-connected cases, whereas the ^{29}Si isotropic chemical shifts show a non-linear behavior when a distribution of Q^n species are present. Overall, the origins of the Raman bands of mineral phases remain poorly known and key mineral groups should be targeted in future studies that combine quantum mechanical and experimental approaches (e.g. this study; Stangarone et al. 2016; Gomes et al. 2021). This work emphasizes the complementary information available using both spectroscopic techniques.

5 Implications

5.1 Raman modes of Q^n species in silicate glasses and melts

Both Raman results and DFT-based calculations highlight that the stretching modes increase in frequency with increasing the number of BO atoms (McMillan 1984; Rossano and Mysen 2012; Nesbitt et al. 2017b; Gomes et al. 2021). Moreover, we may now refine 'the Q^n bands' as they are not related to the entire tetrahedral site but dominantly related to specific Si-O vibrations. While in the hetero-connected phases there are always extra vibrational modes related to the many Si-O bonds in these structures, which cause peaks to overlap, the most intense features correspond to the main structural units. Our results display clear structural trends, permitting future studies linking Raman frequencies to the specific distortions present for a given group of the Q^n species. Moreover, we hope this aids in further distinction among the major mineral groups.

When investigating unpolarized Raman spectra it is typically assumed that the most intense features have A_g symmetry. However, the barium silicates show that the intense Raman peaks display usually, but not exclusively, of A_g symmetry. For example, the vibrational modes of the Q^n species discussed above for BS, B5S8, and H-BS2 are indeed A_g modes (e.g., Fig. 4B), however, the intense high-frequency modes in B2S and low-BS2 have B_{3g} and B_{1g} symmetries, respectively (see tables in supplementary material). This may lead to the misconception that similar intensities are produced from similar structural origins. The phases studied above provide no clear correspondence between any peak characteristic and its structural origin. Therefore, we

recommend that future experimental studies focus on polarized spectra in combination with *ab initio* simulations to disclose this dichotomy.

Assuming that the vibrational modes in the crystalline phase have similar origins to those in the glass (c.f. Brawer and White 1975), as has been demonstrated in the case of $BaSi_2O_5$ (Moulton et al. 2018), we offer several critical comments. First, the spectra of barium silicates show that the intense stretching modes may originate from the bonds between Si and either BO or NBO atoms, or both. This inference was also reported in simulations of Na-silicate glasses (Kilymis et al. 2019). This information should be used to offer more circumspect mode assignments for glass spectra as the stretching modes can be assigned to the Q^n species but attributions to bonds between Si and specific oxygen atoms, or the whole tetrahedron, should be treated with skepticism unless they are traced directly from bands having a known origin in an isochemical crystal phase. Likewise, assignments relating antisymmetric versus symmetric stretching modes appear to no longer be justified for the high-frequency modes, which tend to be localized to specific bonds and not on the entire tetrahedron. Second, B_g and other lower-symmetry modes can have high Raman scattering intensities. This insight may be important in polarized studies of silicate glasses and melts which show that the depolarization ratio changes as the frequencies deviate from the main Q^n peak center (e.g. Kalampounias et al. 2006, 2009). Therefore, non-A_g modes, comparable to those described here, may provide an explanation for the 'extra peaks' needed to fit the glass spectrum.

Finally, the present findings may serve as a guide for more refined and insightful interpretation of Raman spectra in silicates. For instance, the degree of site distortion, as indicated by the Si-O bond lengths and inter-tetrahedral angles, appears to be related to the frequency within the range observed for individual Q^n units. For example, the Q^2 peak positions in both the NMR and Raman spectra above are very close to the limit of the expected Q^2 range and we know that the Q^2-bearing phase, BS, is at the limit of structural stability for the binary barium silicates. When vibrational modes approach these limits, the structure suffers a symmetry breaking process to accommodate a new lower energy configuration.

6 Acknowledgements

BJAM, TRC and CD are grateful to the São Paulo Research Foundation (FAPESP) for funding this research through post doctoral fellowship grants: 2016/18567-5, 2019/12383-8 and 2017/06649-0. The work was further supported by FAPESP grant number 2013/07793-6. We appreciate the support of CNPq and CAPES support to PSP. BJAM would like to thank Harold Lozano (NMR experiments), Millena Logrado (precursor NMR data reduction), and Valmor Mastelaro for making this collaboration possible. EOG acknowledges Generalitat Valenciana for the Santiago Grisolia program (2018/064). EOG and JA acknowledge financial support from Universitat Jaume I, for project UJI-B2019-30. EOG, JA, and LG appreciate support from the Ministerio de Ciencia, Innovación y Universidades (Spain) project PGC2018-094417-B-I00. We also wish to thank the Servei d'Informática, Universitat Jaume I, for their generous allocation of computer time. We would like to thank Mario Tribaudino and the referees for their critical comments which have and will continue to improve this research.

7 References

Aliatis, I., Lambruschi, E., Mantovani, L., Bersani, D., Andò, S., Diego Gatta, G., Gentile, P., Salvioli-Mariani, E., Prencipe, M., Tribaudino, M., and others (2015) A comparison between ab initio calculated and measured Raman spectrum of triclinic albite (NaAlSi3O8). Journal of Raman Spectroscopy, 46, 501–508.

Antao, S.M., Hassan, I., Wang, J., Lee, P.L., and Toby, B.H. (2008) State-of-the-art high-resolution powder X-ray diffraction (HRPXRD) illustrated with Rietveld structure refinement of quartz, sodalite, tremolite, and meionite. The Canadian Mineralogist, 46, 1501–1509.

Apopei, A.I., and Buzgar, N. (2010) The Raman study of amphiboles. Al. I. Cuza Iasi Geologie, 56, 57–83.

Ashbrook, S.E., Le Pollès, L., Pickard, C.J., Berry, A.J., Wimperis, S., and Farnan, I. (2007) First-principles calculations of solid-state 17O and 29Si NMR spectra of Mg2SiO4 polymorphs. Physical Chemistry Chemical Physics, 9, 1587–1598.

Bender, S., Franke, R., Hartmann, E., Lansmann, V., Jansen, M., and Hormes, J. (2002) X-ray absorption and photoemission electron spectroscopic investigation of crystalline and amorphous barium silicates. Journal of Non-Crystalline Solids, 298, 99–108.

Bispo, A.G., Ceccato, D.A., Lima, S.A.M., and Pires, A.M. (2017) Red phosphor based on Eu 3+ -isoelectronically doped Ba 2 SiO 4 obtained via sol-gel route for solid state lightning. RSC Advances, 7, 53752–53762.

Brawer, S.A., and White, W.B. (1975) Raman spectroscopic investigation of the structure of

539 silicate glasses: I. The binary alkali silicates. The Journal of Chemical Physics, 63, 2421–
540 2432.

541 Brown, I.D., and Altermatt, D. (1985) Bond-valence parameters obtained from a systematic
542 analysis of the Inorganic Crystal Structure Database. Acta Crystallographica Section B
543 Structural Science, 41, 244–247.

544 Brown, P.A. (1978) Xonotlite: a New Occurrence At Rose Blanche, Newfoundtand. Canadian
545 Mineralogist, 16, 67–672.

546 Calas, G., Henderson, G.S., and Stebbins, J.F. (2006) Glasses and melts: linking geochemistry to
547 materials science. Elements, 2, 265–268.

548 Charpentier, T., Menziani, M.C., and Pedone, A. (2013) Computational simulations of solid state
549 NMR spectra: A new era in structure determination of oxide glasses. RSC Advances, 3,
550 10550–10578.

551 Chen, M., Xia, Z., Molokeev, M.S., and Liu, Q. (2015) Insights into Ba4Si6O16 structure and
552 photoluminescence tuning of Ba4Si6O16:Ce3+,Eu2+ phosphors. Journal of Materials
553 Chemistry C, 3, 12477–12483.

554 Chopelas, A. (1991) Single crystal Raman spectra of forsterite, fayalite, and monticellite.
555 American Mineralogist, 76, 1101–1109.

556 Cormier, L., Gaskell, P.H., and Creux, S. (1999) Comparison of the low-Q features in diffraction
557 data for silicate glasses and crystals containing Sr or Ba. Journal of Non-Crystalline Solids,
558 248, 84–91.

559 Day, M.C., and Hawthorne, F.C. (2020) A structure hierarchy for silicate minerals: chain, ribbon,
560 and tube silicates. Mineralogical Magazine, 84, 165–244.

561 De Jong, B.H.W.S., Supèr, H.T.J., Spek, A.L., Veldman, N., Nachtegaal, G., and Fischer, J.C.
562 (1998) Mixed Alkali Systems: Structure and 29Si MAS NMR of Li2Si2O5 and K2Si2O5.
563 Acta Crystallographica Section B: Structural Science, 54, 568–577.

564 Denault, K.A., Brgoch, J., Kloß, S.D., Gaultois, M.W., Siewenie, J., Page, K., and Seshadri, R.
565 (2015) Average and local structure, debye temperature, and structural rigidity in some oxide
566 compounds related to phosphor hosts. ACS Applied Materials and Interfaces, 7, 7264–7272.

567 Douglass, R.M. (1958) The crystal structure of sanbornite, BaSi2O5. American Mineralogist, 43,
568 517–536.

569 Dovesi, R., Erba, A., Orlando, R., Zicovich-Wilson, C.M., Civalleri, B., Maschio, L., Rérat, M.,
570 Casassa, S., Baima, J., Salustro, S., and others (2018) Quantum-mechanical condensed
571 matter simulations with CRYSTAL. Wiley Interdisciplinary Reviews: Computational
572 Molecular Science, 8, e1360.

573 Dowty, E. (1987) Vibrational interactions of tetrahedra in silicate glasses and crystals - I.
574 calculations on ideal silicate-aluminate-germanate structural units. Physics and Chemistry
575 of Minerals, 14, 80–93.

576 Eskola, P. (1922) The silicates of strontium and barium. American Journal of Science, 5–4, 331–

375.

Frost, R.L., Mahendran, M., Poologanathan, K., and Xi, Y. (2012) Raman spectroscopic study of the mineral xonotlite Ca6Si6O17(OH)2 - A component of plaster boards. Materials Research Bulletin, 47, 3644–3649.

Gabelica-Robert, M., and Tarte, P. (1979) Vibrational spectrum of akermanite-like silicates and germanates. Spectrochimica Acta Part A: Molecular Spectroscopy, 35, 649–654.

——— (1981) Vibrational spectrum of fresnoite (Ba2TiOSi2O7) and isostructural compounds. Physics and Chemistry of Minerals, 7, 26–30.

Gagné, O.C., and Hawthorne, F.C. (2015) Comprehensive derivation of bond-valence parameters for ion pairs involving oxygen. Acta Crystallographica Section B Structural Science, Crystal Engineering and Materials, 71, 562–578.

Gibbs, G. V., Cox, D.F., Ross, N.L., Crawford, T.D., Burt, J.B., and Rosso, K.M. (2005) A mapping of the electron localization function for earth materials. Physics and Chemistry of Minerals, 32, 208–221.

Gomes, E.O., Fabris, G.S.L., Ferrer, M.M., Motta, F. V., Bomio, M.R.D., Andres, J., Longo, E., and Sambrano, J.R. (2019) Computational procedure to an accurate DFT simulation to solid state systems. Computational Materials Science, 170, 109176.

Gomes, E.O., Moulton, B.J.A., Cunha, T.R., Gracia, L., Pizani, P.S., and Andrés, J. (2021) Identifying and explaining vibrational modes of sanbornite (low-BaSi2O5) and Ba5Si8O21: A joint experimental and theoretical study. Spectrochimica Acta Part A: Molecular and Biomolecular Spectroscopy, 248, 119130.

Gorelova, L.A., Bubnova, R.S., Krivovichev, S. V., Krzhizhanovskaya, M.G., and Filatov, S.K. (2016) Thermal expansion and structural complexity of Ba silicates with tetrahedrally coordinated Si atoms. Journal of Solid State Chemistry, 235, 76–84.

Greaves, G.N. (1985) EXAFS and the structure of glass. Journal of Non-Crystalline Solids, 71, 203–217.

Grosse, H.-P., and Tillmanns, E. (1974a) Barium metasilicate BaSiO3 (h). Crystal Structure Communications, 3, 603–605.

——— (1974b) Barium orthosilicate Ba2SiO4. Crystal Structure Communications, 3, 599–601.

Handke, M., and Urban, M. (1982) IR and Raman spectra of alkaline earth metals orthosilicates. Journal of Molecular Structure, 79, 353–356.

Hawthorne, F.C., and Grundy, H.D. (1976) The Crystal Chemistry of the Amphiboles: IV. X-ray and Neurton refinements of the crystal structure of tremolite. Canadian Mineralogist, 14, 334–345.

Hawthorne, F.C., Uvarova, Y.A., and Sokolova, E. (2019) A structure hierarchy for silicate minerals: sheet silicates. Mineralogical Magazine, 83, 3–55.

Hejny, C., and Armbruster, T. (2001) Polytypism in xonotlite Ca6Si6O17(OH)2. Zeitschrift fur Kristallographie, 216, 396–408.

Hesse, K.F., and Liebau, F. (1980a) Crystal chemistry of silica-rich Barium silicates I: Refinement of the crystal structures of Ba4[Si6O16], Ba5[Si8O21] and Ba6[Si10O26], silicates with triple, quadruple and quintuple chains. Zeitschrift fur Kristallographie - New Crystal Structures, 153, 3–17.

——— (1980b) Crystal chemistry of silica-rich Barium silicates III: Refinement of the crystal structures of the layer silicates Ba2[Si4O10] (I), (Sanbornite), and Ba2[Si4O10] (h). Zeitschrift fur Kristallographie - New Crystal Structures, 153, 33–41.

Huang, E., Chen, C.H., Huang, T., Lin, E.H., and Xu, J.A. (2000) Raman spectroscopic characteristics of Mg-Fe-Ca pyroxenes. American Mineralogist, 85, 473–479.

Kalampounias, A.G., Yannopoulos, S.N., and Papatheodorou, G.N. (2006) Temperature- induced structural changes in glassy, supercooled, and molten silica from 77 to 2150 K. J. Chem. Phys., 124, 14504.

Kalampounias, A.G., Nasikas, N.K., and Papatheodorou, G.N. (2009) Glass formation and structure in the MgSiO3–Mg2SiO4 pseudobinary system: From degraded networks to ioniclike glasses. The Journal of Chemical Physics, 131, 114513.

Kilymis, D., Ispas, S., Hehlen, B., Peuget, S., and Delaye, J.M. (2019) Vibrational properties of sodosilicate glasses from first-principles calculations. Physical Review B, 99, 1–14.

Kinsey, R.A., Kirkpatrick, R.J., Hower, J., Smith, K.A., and Oldfield, E. (1985) High Resolution Aluminum-27 and Silicate-29 Nuclear Magnetic resonance spectroscopic study of layer silicates, including clay minerals. American Mineralogist, 70, 537–548.

Konijnendijk, W.L., and Stevels, J.M. (1976) Raman scattering measurements of silicate glasses and compounds. Journal of Non-Crystalline Solids, 21, 447–453.

Kudoh, Y., and Takéuchi, Y. (1979) Polytypism of xonotlite: (I) Structure of an A-1 polytype. Mineralogical Journal, 9, 349–373.

Lafuente, B., Downs, R.T., Yang, H., and Stone, N. (2015) The power of databases: the RRUFF project., 1–30 p. (T. Armbruster & R.M. Danisi, Eds.)Highlights in Mineralogical Crystallography Vol. pp. 1-30. W. De Gruyter.

Lam, P.K., Yu, R., Lee, M.W., and Sharma, S.K. (1990) Structural distortions and vibrational modes in Mg2SiO4. American Mineralogist, 75, 109–119.

Larson, A.C., and Von Dreele, R.B. (2004) General Structure Analysis System (GSAS). Los Alamos National Laboratory Report LAUR, 748, 86–748.

Liebau, F. (1985) Structural Chemistry of Silicates, 1st ed., 347 p. Springer Berlin Heidelberg, Berlin, Heidelberg.

Lin, S., Lin, H., Huang, Q., Cheng, Y., Xu, J., Wang, J., Xiang, X., Wang, C., Zhang, L., and Wang, Y. (2019) A Photostimulated BaSi2O5 :Eu2+ ,Nd3+ Phosphor-in-Glass for Erasable-Rewritable Optical Storage Medium. Laser & Photonics Reviews, 13, 1900006.

Mägi, M., Lippmaa, E., Samoson, A., Engelhardt, G., and Grimmer, A.R. (1984) Solid-state high-resolution silicon-29 chemical shifts in silicates. Journal of Physical Chemistry, 88,

1518–1522.

Mantovani, L., Tribaudino, M., Aliatis, I., Lambruschi, E., Lottici, P.P., and Bersani, D. (2015) Raman spectroscopy of CaCoSi2O6–Co2Si2O6 clinopyroxenes. Physics and Chemistry of Minerals, 42, 179–189.

Massiot, D., Fayon, F., Capron, M., King, I., Le Calvé, S., Alonso, B., Durand, J.O., Bujoli, B., Gan, Z., and Hoatson, G. (2002) Modelling one- and two-dimensional solid-state NMR spectra. Magnetic Resonance in Chemistry, 40, 70–76.

McGinnety, J.A. (1972) Redetermination of the structures of potassium sulphate and potassium chromate: the effect of electrostatic crystal forces upon observed bond lengths. Acta Crystallographica Section B Structural Crystallography and Crystal Chemistry, 28, 2845–2852.

McKeown, D.A., and Bell, M.I. (1998) Linked four-membered silicate rings: Vibrational analysis of Gillespite: BaFeSi4O10 and implications for glass structure. Physics and Chemistry of Minerals, 25, 273–281.

McMillan, P. (1984) Structural studies of silicate glasses and melts--applications and limitations of Raman spectroscopy. American Mineralogist, 69, 622–644.

Mohanan, K., Sharma, S.K., and Bishop, E.C. (1993) A Raman spectral study of forsterite-monticellite solid solutions. American Mineralogist, 78, 42–48.

Moulton, B.J.A., Rodrigues, A.M., Pizani, P.S., Sampaio, D.V., and Zanotto, E.D. (2018) A Raman investigation of the structural evolution of supercooled liquid barium disilicate during crystallization. International Journal of Applied Glass Science, 9, 510–517.

Moulton, B.J.A., Rodrigues, A.M., Sampaio, D. V., Silva, L.D., Cunha, T.R., Zanotto, E.D., and Pizani, P.S. (2019) The origin of the unusual DSC peaks of supercooled barium disilicate liquid. CrystEngComm, 21, 2768–2778.

Murdoch, J.B., Stebbins, J.F., and Carmichael, I.S.E. (1985) High resolution ^29Si NMR study of silicate and aluminosilicate glasses: the effect of network-modifying cations. American Mineralogist, 70, 332–343.

Nada, R., Nicholas, J.B., McCarthy, M.I., and Hess, A.C. (1996) Basis sets for ab initio periodic Hartree—Fock studies of zeolite/adsorbate interactions: He, Ne, and Ar in silica sodalite. International Journal of Quantum Chemistry, 60, 809–820.

Namwong, P., Laorodphan, N., Thiemsorn, W., Jaimasith, M., Wannakon, A., and Chairuangsri, T. (2010) A barium-calcium silicate glass for use as seals in planar SOFCs. Chiang Mai Journal of Science, 37, 231–242.

Nesbitt, H.W., Henderson, G.S., and Bancroft, G.M. (2017a) Electron densities over Si and O atoms of tetrahedra and their impact on Raman stretching frequencies and Si-NBO force constants. Chemical Geology, 461, 65–74.

——— (2017b) Electron densities over Si and O atoms of tetrahedra and their impact on Raman stretching frequencies and Si-NBO force constants. Chemical Geology, 461, 65–74.

691 Nesbitt, H.W., Bancroft, G.M., and Henderson, G.S. (2018) Temperature dependence of Raman
692 shifts and line widths for Q0 and Q2 crystals of silicates, phosphates, and sulfates.
693 American Mineralogist, 103, 966–976.

694 Nesbitt, H.W., Henderson, G.S., Bancroft, G.M., and Neuville, D.R. (2020) Spectral Resolution
695 and Raman Q and Q cross sections. Chemical Geology, 562, 120040.

696 Oehlschlegel, G. (1975) Crystallization of Glasses in the System BaO*2SiO2-2BaO*3SiO2.
697 Journal of the American Ceramic Society, 58, 148–149.

698 Ott, J.N., and Williams, Q. (2020) Raman spectroscopic constraints on compression and
699 metastability of the amphibole tremolite at high pressures and temperatures. Physics and
700 Chemistry of Minerals, 47, 27.

701 Pedone, A., Charpentier, T., and Menziani, M.C. (2010) Multinuclear NMR of CaSiO3 glass:
702 simulation from first-principles. Physical Chemistry Chemical Physics, 12, 6054–6066.

703 Piriou, B., and McMillan, P.F. (1983) The high-frequency vibrational spectra of vitreous and
704 crystalline orthosilicates. American Mineralogist, 68, 426–443.

705 Richet, P., Mysen, B.O., and Ingrin, J. (1998) High-temperature X-ray diffraction and Raman
706 spectroscopy of diopside and pseudowollastonite. Physics and Chemistry of Minerals, 25,
707 401–414.

708 Rietveld, H.M. (1967) Line profiles of neutron powder-diffraction peaks for structure
709 refinement. Acta Crystallographica, 22, 151–152.

710 Rossano, S., and Mysen, B. (2012) Raman spectroscopy of silicate glasses and melts in
711 geological systems. European Mineralogical Union Notes in Mineralogy, 12, 321–366.

712 Roth, R.S., and Levin, E.M. (1959) Phase equilibria in the subsystem barium disilicate -
713 dibarium trisilicate. Journal of Research of the National Bureau of Standards, 62, 193.

714 Schlenz, H., Kirfel, A., Schulmeister, K., Wartner, N., Mader, W., Raberg, W., Wandelt, K.,
715 Oligschleger, C., Bender, S., Franke, R., and others (2002) Structure analyses of Ba-silicate
716 glasses. Journal of Non-Crystalline Solids, 297, 37–54.

717 Sherriff, B.L., and Grundy, H.D. (1988) Calculations of 29Si MAS NMR chemical shift from
718 silicate mineral structure. Nature, 332, 819–822.

719 Shukla, A., Jung, I.-H., Decterov, S.A., and Pelton, A.D. (2018) Thermodynamic evaluation and
720 optimization of the BaO-SiO2 and BaO-CaO-SiO2 systems. Calphad, 61, 140–147.

721 Smith, K.A., Kirkpatrick, R.J., and Henderson, D.M. (1983) High-resolution silicon-29 nuclear
722 magnetic resonance study of rock-forming silicates. American Mineralogist, 68, 1206–
723 1215.

724 Stangarone, C., Tribaudino, M., Prencipe, M., and Lottici, P.P. (2016) Raman modes in Pbca
725 enstatite (Mg2Si2O6): an assignment by quantum mechanical calculation to interpret
726 experimental results. Journal of Raman Spectroscopy, 47, 1247–1258.

727 Stangarone, C., Böttger, U., Bersani, D., Tribaudino, M., and Prencipe, M. (2017) Ab initio
728 simulations and experimental Raman spectra of Mg2SiO4 forsterite to simulate Mars

729 surface environmental conditions. Journal of Raman Spectroscopy, 48, 1528–1535.

730 Takahashi, Y., Osada, M., Masai, H., and Fujiwara, T. (2010) Transmission electron microscopy
731 and in situ Raman studies of glassy sanbornite: An insight into nucleation trend and its
732 relation to structural variation. Journal of Applied Physics, 108, 63507.

733 Tarte, P., Pottier, M.J., and Procès, A.M. (1973) Vibrational studies of silicates and germanates-
734 V. I.R. and Raman spectra of pyrosilicates and pyrogermanates with a linear bridge.
735 Spectrochimica Acta Part A: Molecular Spectroscopy, 29, 1017–1027.

736 Thompson, L.M., McCarty, R.J., and Stebbins, J.F. (2012) Estimating accuracy of 17O NMR
737 measurements in oxide glasses: Constraints and evidence from crystalline and glassy
738 calcium and barium silicates. Journal of Non-Crystalline Solids, 358, 2999–3006.

739 Towler, M.D. (1996) Barium basis sets for the CRYSTAL program.

740 Tribaudino, M., Mantovani, L., Bersani, D., and Lottici, P.P. (2012) Raman spectroscopy of
741 (Ca,Mg)MgSi2O6 clinopyroxenes. American Mineralogist, 97, 1339–1347.

742 Tribaudino, M., Stangarone, C., Gori, C., Mantovani, L., Bersani, D., and Lottici, P.P. (2019)
743 Experimental and calculated Raman spectra in Ca–Zn pyroxenes and a comparison between
744 (CaxM2+1−x)M2+Si2O6 pyroxenes (M2+ = Mg, Co, Zn, Fe2+). Physics and Chemistry of
745 Minerals, 46, 827–837.

746 Valenzano, L., Torres, F.J., Doll, K., Pascale, F., Zicovich-Wilson, C.M., and Dovesi, R. (2006)
747 Ab Initio Study of the Vibrational Spectrum and Related Properties of Crystalline
748 Compounds; the Case of CaCO3 Calcite. Zeitschrift für Physikalische Chemie, 220, 893–
749 912.

750 Voronko, Y.K., Sobol, A.A., and Shukshin, V.E. (2006) Raman spectra and structure of silicon-
751 oxygen groups in crystalline, liquid, and glassy Mg 2SiO 4. Inorganic Materials, 42, 981–
752 988.

753 Walstrom, R.E., and Leising, J.F. (2005) Barium minerals of the Sanbornite Deposits. Axis, 1, 1–
754 18.

755 Wang, A., Freeman, J.J., and Jolliff, B.L. (2015) Understanding the Raman spectral features of
756 phyllosilicates. Journal of Raman Spectroscopy, 46, 829–845.

757 Xiao, F., Xue, Y.N., and Zhang, Q.Y. (2009) Bluish-green color emitting Ba2Si3O8:Eu2+
758 ceramic phosphors for white light-emitting diodes. Spectrochimica Acta - Part A: Molecular
759 and Biomolecular Spectroscopy, 74, 758–760.

760 Zicovich-Wilson, C.M., Pascale, F., Roetti, C., Saunders, V.R., Orlando, R., and Dovesi, R.
761 (2004) Calculation of the vibration frequencies of α-quartz: The effect of Hamiltonian and
762 basis set. Journal of Computational Chemistry, 25, 1873–1881.

763

764

765 **Figure captions:**

766 **Figure 1:** Structural features of the barium silicate phases showing homo-connected (top) and
767 hetero-connected (bottom) phases. Below each structure is their composition and Q^n species. For
768 the hetero-connected phases black triangles representing the tetrahedra across the ribbon
769 structure, are labelled with both their Q^n species (left-side triangles) and Si site number (right-
770 side). The structures contain Si (small blue), Ba (yellow), bridging oxygen (brown) and non-
771 bridging oxygens (red). Ba cations have been omitted for clarity in the hetero-connected
772 structures.

773

774 **Figure 2:** Diffractogram and Rietveld refinement of B6S10. The 'x' symbols are the
775 experimental measured values, the red solid line represents the calculated intensities from
776 Rietveld refinement and the blue solid line at the bottom is the residual curve between them.

777

778 **Figure 3:** ^{29}Si MAS NMR spectra of crystalline phases. Dashed lines are placed at -93.1 (homo-
779 connected Q^3) and -80.0 ppm (homo-connected Q^2). The weak additional resonances observed in
780 sample B5S8 arise from minor impurities of B6S10.

781

782 **Figure 4:** Representative Raman spectra of the bending (a) and stretching (b) regions of
783 crystalline barium silicates. Black marks below spectra indicate the theoretically calculated
784 frequency of the mode. Spectra are in the same order in both panels. Numbers inside triangles
785 correspond to vibrations depicted to the righthand side.

786

787 **Figure 5:** Chemical shift versus inter-tetrahedral angle for phases with Q^2 and Q^3 species. Error
788 bars are smaller than the symbols.

789

790 **Figure 6:** ^{29}Si MAS NMR chemical shift versus composition. Homo-connected barium silicate
791 are shown as hollow red circles. Hetero-connected barium silicates are shown as filled circles in
792 green for Q^3 and blue for Q^2. The data sources are reported in supplemental materials section
793 S5.1. Structural units are plotted by O:Si ratio showing Q^0 as 'X', Q^1 as squares, Q^2 as '+', Q^3 as
794 triangles and Q^4 as '—'. Lighter shades of these symbols indicate Al-bearing phases. Hetero-
795 connected tremolite and xonotlite are shown as purple diamonds.

796

797 **Figure 7:** Raman scattering wavenumber of the Si-O stretching modes versus composition. Peak
798 positions from this study are plotted as circles (open for homo-connected Q^n species; solid green
799 (Q^3) or blue (Q^2) for hetero-connected Q^n phases). Database values are for nesosilicates, Q^0,
800 (blue x), sorosilicates, Q^1, (orange squares), inosilicates, Q^2, (grey +), and phyllosilicates, Q^3

(yellow triangles). Purple diamonds refer to tremolite and xonotlite. The central lines and bars on the righthand side correspond to the mean Q^n position and $\pm 1\sigma$ of their distribution.

Figure 8: Raman wavenumber versus ^{29}Si chemical shift for the barium silicate phases. Note the trends within Q^2 and Q^3 resonances which are orthogonal to the general positive correlation observed for the Q^n species with chemical and Raman shifts.

This is the peer-reviewed, final accepted version for American Mineralogist, published by the Mineralogical Society of America.
The published version is subject to change. Cite as Authors (Year) Title. American Mineralogist, in press.
DOI: https://doi.org/10.2138/am-2021-7910. http://www.minsocam.org/

Table 1: Values of crystal structural parameters .

Phase ID	Formula	BaO mol. %	O:Si	ICSD[1]	Space Group		Density (g/cm^3) theoretical	Density (g/cm^3) experimental	Cell Volume Å^3	a Å	b Å	c Å	β °	# of Sites (Wyckoff)	Ba CN_{PFU}[2]	Reference[3]
				6246			5.49		444.02	5.805	10.200	7.499	90.00			[i]
				291355			5.466		445.56	5.810	10.217	7.506	90.00	Ba: 2 (4 c)		[ii]
B2S	Ba_2SiO_4	66.6	4		Pmcn	62			444.76	5.807	10.209	7.503	90.00	Si: 1 (4 c)	9.5	[iii]
							5.464		**445.81(2)**	**5.811**	**10.220**	**7.507**	**90.00**			**This study - Rietveld**
							5.303		**460.62**	**5.861**	**10.358**	**7.586**	**90.00**			**This study - DFT**
				6245			4.44		319.46	4.580	5.611	12.431	90.00			[iv]
									320.30	4.584	5.616	12.443	90.00	Ba: 1 (4 a)		[iii]
high-BS	$BaSiO_3$	50	3		$P2_12_12_1$	19								Si: 1 (4 a)	8	
							4.419		**320.79(1)**	**4.585**	**5.619**	**12.450**	**90.00**			**This study - Rietveld**
							4.277		**322.13**	**4.616**	**5.692**	**12.260**	**90.00**			**This study - DFT**
				100310			3.98	3.97	813.54	12.477	4.685	13.944	93.54			[v]
									814.0	12.483	4.686	13.943	93.53	Ba: 2 (4 e)		[iii]
B4S6	$Ba_4Si_6O_{16}$	40	2.67		$P2_1/c$	14								Si: 3 (4 e)	8.5	
							3.976		**813.46(6)**	**12.477**	**4.685**	**13.943**	**93.58**			**This study - Rietveld**
							3.838		**844.11**	**12.652**	**4.725**	**14.147**	**93.73**			**This study - DFT**
				100311			3.925	3.93	2110.20	32.675	4.695	13.894	98.10			[v]
									2120.6	32.739	4.702	13.917	98.17	Ba: 1+2 (8 f, 4 a)	8	[iii]
B5S8	$Ba_5Si_8O_{21}$	38.5	2.63		C2/c	15								Si: 4 (8 f)	(*7.6)	Rietveld - [vii]
							3.905		**2121.6(2)**	**32.756**	**4.705**	**13.909**	**98.18**			DFT - [vii]
							3.771		**2200.25**	**33.284**	**4.738**	**14.097**	**98.29**			
				100312			3.882	3.88	1301.03	20.196	4.707	13.842	98.61	Ba: 3 (4 e)		[v]
B6S10	$Ba_6Si_{10}O_{26}$	37.5	2.6		$P2_1/c$	14								Si: 5 (4 e)	8.33	
							3.876		**1303.28(7)**	**20.210**	**4.707**	**13.856**	**98.63**			**This study - Rietveld**
				100314			3.74	3.74	1457.96	23.195	4.658	13.613	97.57			[vi]
									1459.0	23.193	4.659	13.622	97.56	Ba: 2 (4 a, 8 f)		[iii]
high-BS2	$BaSi_2O_5$	33.3	2.5		C2/c	15								Si: 3 (8 f)	8.67	
							3.720		**1465.17(7)**	**23.232**	**4.665**	**13.637**	**97.55**			**This study - Rietveld**
							3.604		**1513.92**	**23.466**	**4.702**	**13.842**	**97.61**			**This study - DFT**
				100313			3.77	3.70	481.25	7.688	4.629	13.523	90.00			[vi]
									481.78	7.690	4.632	13.528	90.00	Ba: 1 (4 c)		[iii]
Sanbornite (low-BS2)	$BaSi_2O_5$	33.3	2.5		Pmcn	62								Si: 1 (8 d)	9	Rietveld - [vii]
							3.762		**482.94(2)**	**7.696**	**4.636**	**13.538**	**90.00**			
							3.632		**500.84**	**7.778**	**4.684**	**13.744**	**90.00**			DFT - [vii]

* Note that Rietveld model standard deviation, when not shown (e.g. lattice parameters), are less than ±1 of the last decimal place reported.

[1] International Crystal Structure Database (ICSD) available: https://www.fiz-karlsruhe.de/; densities also come from the data reported in ICSD.

[2] PFU - per formula unit. For example, high-BS2 has two sites with different multiplicity: CN_{PFU} = (4*8 + 8*9)/12 = 8.67). Ba-O cutoff radius is 3.3 Å. Ba CN = 7.6 for B5S8 if the two O at 3.27 Å are excluded.

[3] references: [i] Grosse & Tillmanns, 1974b; [ii] Denault et al., 2015; [iii] Gorelova et al., 2016; [iv] Grosse & Tillmanns, 1974a; [v] Hess & Liebau, 1980b; [vi] Hess & Liebau, 1980a; [vii] Gomes et al., 2021.

This is the peer-reviewed, final accepted version for American Mineralogist, published by the Mineralogical Society of America.
The published version is subject to change. Cite as Authors (Year) Title. American Mineralogist, in press.
DOI: https://doi.org/10.2138/am-2021-7910. http://www.minsocam.org/

Table 2: Values of peak parameters obtained by ^{29}Si MAS NMR spectroscopy .

Si Site		1		2		3		4		5		
Phase	**Q^n**	Shift ppm	Area %	Shift ppm	Area %	Shift ppm	Area %	Shift ppm	Area %	Shift ppm	Area %	**Reference[1]**
low-BS2	Q^3	-93.11	100									
		-93.5										[i]
high-BS2	Q^3	-93.03	66.5	-92.11	33.5							
B6S10	Q^2-4Q^3	-93.02	19.7	-92.18	20.3	-88.84	18.9	-87.97	20.2	-81.37	21.0	
B5S8	Q^2-3Q^3	-94.14	23.9			-89.60	52.2			-81.42	23.9	
B4S6	Q^2-2Q^3	-92.18	35.8	-91.22	32.1					-81.20	32.1	
high-BS	Q^2									-80.00	100	
										-80		[ii]
B2S	Q^0									-70.12	100	
										-70.3		[iii]

*** Notes: i) frequency resolution is 0.03 ppm; ii) peak FWHM fixed to the value of L-BS2 = 1.11 ppm.**

[1] References: [i] Murdoch et al., 1985; [ii] Smith et al., 1985; [iii] Mägi et al., 1984.

This is the peer-reviewed, final accepted version for American Mineralogist, published by the Mineralogical Society of America.
The published version is subject to change. Cite as Authors (Year) Title. American Mineralogist, in press.
DOI: https://doi.org/10.2138/am-2021-7910. http://www.minsocam.org/

Table 3: Values of peak parameters obtained by Raman spectroscopy .

		***Bending* region**				***Stretching* region**						
Phase	**Q^n**	Center cm^{-1}	FWHM cm^{-1}	Center cm^{-1}	FWHM cm^{-1}	Center cm^{-1}	FWHM cm^{-1}	Center cm^{-1}	FWHM cm^{-1}	Center cm^{-1}	FWHM cm^{-1}	**Note**[1]
low-BS2	**Q^3**	**535.5**	**8.2**					**1077.9**	4.5			this study
	Q^3	535.2	8.5					1076.8	4.6			1
Sanbornite	**Q^3**	535.1	8.8					1076.9	4.6			1
high-BS2	**Q^3**	**533.8**	**8.5**					**1079.5**	5.2			this study
	Q^3	533.5	8.8					1079.2	5.4			1
B6S10	**Q^2:4Q^3**	**534.7**	**7.0**	544.3	5.4	**921.3**	7.9	**1069.2**	6.3	1075.3	4.5	this study
σ		0.1	0.6	0.5	0.9	0.1	0.5	**0.2**	0.3	0.1	0.3	
B6S10	**Q^2:4Q^3**	535.6	6.5	546.1	4.9	924.6	6.2	1067.0	5.5	1075.3	6.8	1
B5S8	**Q^2:3Q^3**	**535.1**	**6.6**	545.7	5.3	**924.0**	7.2	**1066.8**	5.5	1075.3	4.5	this study
		535.6	6.0	545.8	4.4	923.6	6.4	1065.6	5.5			1
B4S6	**Q^2:2Q^3**	**532.0**	**5.5**	549.1	5.1	**928.1**	6.6	**1061.0**	5.0	1049.9	7.3	this study
high-BS	**Q^2**	**599.8**	**9.7**			**964.0**	8.3					this study
B2S[3]	**Q^0**					**823.7**	3.2	858.4	6.2			this study

[1] 1 come from Moulton et al., 2019 based on a 'local' fit and samples of H-BS2, B5S8 and B6S10 were those of Gorelova et al., (2016).

[2] σ values were calculated from the mean of three spectra. Exemplar σ are reported for B6S10 as these values are typical for all fits and larger than phases with fewer Si sites.

[3] Ba_2SiO_4 values were also measured as 822 cm^{-1} by Bispo Jr. et al. (2017) & as 819 cm^{-1} by Handke & Urban, (1982).

* All results were reproduced using 532 and 633 nm lasers & are reproducible within <1.5 cm^{-1}.

This is the peer-reviewed, final accepted version for American Mineralogist, published by the Mineralogical Society of America.
The published version is subject to change. Cite as Authors (Year) Title. American Mineralogist, in press.
DOI: https://doi.org/10.2138/am-2021-7910. http://www.minsocam.org/

Table 4: Experimental and theoretical vibrational modes in barium orthosilicate, Ba_2SiO_4[1].

Raman Modes

Mode	Measured				Theoretical			
	Frequency cm^{-1}	FWHM cm^{-1}	Relative Intensity (%)	Area %	Frequency cm^{-1}	Δν cm^{-1}	Symmetry	Origin[2]
ν_1					56.9		B_{2g}	O1-Ba2,1
ν_2	59.2	1.6	29.1	4.5	63.2	3.9	A_g	Ba1-Ba2
ν_3	68.6	4.2	6.8	2.8	69.1	0.5	B_{1g}	Ba1-Ba2-O2
ν_4	73.0	2.8	9.8	2.6	75.4	2.4	B_{3g}	Ba2-Ba1
ν_5					76.7		B_{2g}	O2-Ba2,1
ν_6	86.4	3.8	9.6	3.6	89.1	2.8	A_g	Ba2-Ba1
ν_7	89.7	3.6	20.1	7.1	92.8	3.1	B_{1g}	Ba1,2
ν_8					96.2		A_g	Ba1-Si
ν_9					105.0		B_{2g}	Ba1-Ba2
ν_{10}	108.9	1.2	9.5	1.1	105.5	-3.4	B_{3g}	Ba1,2
ν_{11}					121.9		A_g	Ba2-O1
ν_{12}	132.2	3.7	0.8	0.3	137.3	5.1	B_{1g}	lattice
ν_{13}					141.9		B_{3g}	O2,3-Ba2
ν_{14}	158.8	7.9	1.5	1.2	158.2	-0.6	A_g	O2-Ba2-O2
ν_{15}					158.4		B_{3g}	Ba2
ν_{16}					159.1		B_{2g}	O2-Ba2
ν_{17}	169.0	6.2	4.8	2.9	169.7	0.7	B_{1g}	O2-Ba2-O2
ν_{18}	181.9	5.8	16.4	9.4	186.0	4.1	B_{3g}	lattice
ν_{19}	195.6	13.8	2.8	3.8	200.4	4.8	B_{2g}	O3-Ba1-Ba2
ν_{20}	207.9	5.1	12.5	6.2	210.4	2.5	A_g	lattice
ν_{21}					213.8		B_{3g}	O2-Ba2-Ba1
ν_{22}					218.6		B_{1g}	O3-Ba1-Ba2
ν_{23}					223.4		A_g	lattice
ν_{24}					258.3		B_{3g}	O1-Ba2,1
ν_{25}	347.5	6.8	0.5	0.3	363.6	16.1	A_g	O1-Ba2
ν_{26}	370.3	10.4	4.6	4.7	377.4	7.1	B_{1g}	lattice
ν_{27}					390.6		B_{2g}	lattice
ν_{28}					393.6		B_{3g}	lattice
ν_{29}	490.3	3.3	1.8	0.6	517.3	27.0	A_g	O3-Si-Ba1
ν_{30}	497.4	3.5	15	5	519.7	22.3	B_{3g}	lattice
ν_{31}	520.7	3.5	1.5	0.5	525.9	5.2	B_{1g}	SiO4
ν_{32}					526.9		B_{2g}	SiO4
ν_{33}					552.8		A_g	lattice
ν_{34}					569.6		B_{3g}	O2-Si-O3
ν_{35}	815.3	6.9	1.1	0.8	827.9	12.6	A_g	O1-Si
ν_{36}	823.7	3.2	100	32	833.4	9.7	B_{3g}	O1-Si
ν_{37}	854.0	3.2	2.0	1	863.3	9.3	A_g	O2-Si-O1
ν_{38}	858.4	6.2	8.4	4.5	876.4	18.0	B_{3g}	SiO4
ν_{39}	867.0	3.4	2.0	0.7	895.5	28.5	B_{1g}	O2-Si
ν_{40}	887.8	5.0	3.9	1.9	895.6	7.8	B_{2g}	O2-Si
ν_{41}	910.2	5.1	6.0	3.0	942.2	32.0	A_g	O2-Si
ν_{42}					966.4		B_{3g}	O3-Si
Mean A_g FWHM*		5.0			|Δν|[3]	7.5		
Mean B_g FWHM*		5.5			maximum Δν	32.0		

* Only modes contributing >1% area were considered.

[1] Note that all O are NBO and the Si site is a Q^0 species.

[2] Mode origin are labelled as 'lattice' where they involve both BaO_x & SiO_4.

[3] |Δν| is the absolute mean difference between theoretical and experimental frequency.

This is the peer-reviewed, final accepted version for American Mineralogist, published by the Mineralogical Society of America.
The published version is subject to change. Cite as Authors (Year) Title. American Mineralogist, in press.
DOI: https://doi.org/10.2138/am-2021-7910. http://www.minsocam.org/

Table 5: Theoretical versus experimental (Exp) $^{-27}$Si MAS NMR chemical shift frequencies.

Si Site	low-$BaSi_2O_5$			high-$BaSi_2O_5$			$Ba_6Si_{10}O_{26}$			$Ba_5Si_8O_{21}$			$Ba_4Si_6O_{16}$			Tremolite[a]	Xonotlite[a]	high-$BaSiO_3$			Ba_2SiO_4		
	Exp	SG88[b]		Exp	SG88		Exp	SG88		Exp	SG88		Exp	SG88		Exp	Exp	Exp	SG88		Exp	SG88	
		3.7 Å	2 NNN		3.7 Å	2 NNN		3.7 Å	2 NNN		3.7 Å	2 NNN		3.7 Å	2 NNN				3.7 Å	2 NNN		3.7 Å	2 NNN
1							**-81.4**	-73.5	-82.4	**-81.4**	-80.4	-83.5	**-81.2**	-73.8	-78.3	-87.8	-86.8	**-80.0**	-72.4	-72.4	**-70.1**	-61.6	-57.6
2							**-88.0**	-88.2	-97.3														
3				**-92.1**	-87.6	-92.4	**-88.8**	-88.8	-88.8	**-89.6**	-91.7	-91.7											
4				**-93.0**	-90.6	-95.4	**-92.2**	-90.9	-98.3	**-89.6**	-92.0	-90.2	**-91.2**	-85.8	-102.5								
5	**-93.1**	-86.3	-87.8	**-93.0**	-91.5	-96.1	**-93.0**	-96.8	-100.0	**-94.1**	-93.0	-96.9	**-92.2**	-92.3	-99.9	-92.2	-97.8						

[a] - chemical shift of tremolite and xonotlite are from Mägi et al., 1984

[b] - SG88 derived values come from the empirical model of Sherriff & Grundy (1988) where the NNN have been limited to either, neighbours up to 3.7 Å (3.7 Å), or two next-nearest neighbours (2 NNN)

This is the peer-reviewed, final accepted version for American Mineralogist, published by the Mineralogical Society of America.
The published version is subject to change. Cite as Authors (Year) Title. American Mineralogist, in press.
DOI: https://doi.org/10.2138/am-2021-7910. http://www.minsocam.org/

Table 6: Values of Si site parameters.

Phase	Q^n	Site Parameter		
		Si-O (Å)	Avg. Si-O-Si (˚)	Volume (Å^3)
B2S	0	**1.633**	n/a	**2.230**
Ba_2SiO_4	0	1.638	n/a	**2.250**
B-BS	2	**1.623**	**128.2**	**2.165**
B2S3	2	**1.636**	**129.7**	**2.219**
$Ba_4Si_6O_{16}$	3	**1.620**	**135.8**	**2.157**
	3	**1.617**	**139.1**	**2.146**
mean		1.624	134.9	2.174
B5S8	2	**1.623**	**132.2**	**2.118**
$Ba_5Si_8O_{21}$	3	**1.604**	**134.8**	**2.045**
	3	**1.612**	**135.6**	**2.123**
	3	**1.608**	**146.5**	**2.212**
mean		1.612	137.3	2.125
B3S5	2	**1.647**	**131.0**	**2.251**
$Ba_6Si_{10}O_{26}$	3	**1.624**	**133.8**	**2.181**
	3	**1.614**	**134.1**	**2.128**
	3	**1.608**	**138.6**	**2.104**
	3	**1.606**	**142.3**	**2.098**
mean		1.620	136.0	2.152
H-BS2	3	**1.619**	**137.6**	**2.151**
$BaSi_2O_5$	3	**1.616**	**138.5**	**2.152**
	3	**1.616**	**138.1**	**2.146**
mean		1.617	138.1	2.150
Sanbornite	3	**1.614**	**138.6**	2.140
Low-Quartz[1]	4	**1.608**	**143.8**	2.134

[1] low-quartz values determined from Antao & Hassan, (2008).

This is the peer-reviewed, final accepted version for American Mineralogist, published by the Mineralogical Society of America.
The published version is subject to change. Cite as Authors (Year) Title. American Mineralogist, in press.
DOI: https://doi.org/10.2138/am-2021-7910. http://www.minsocam.org/

Fig 1

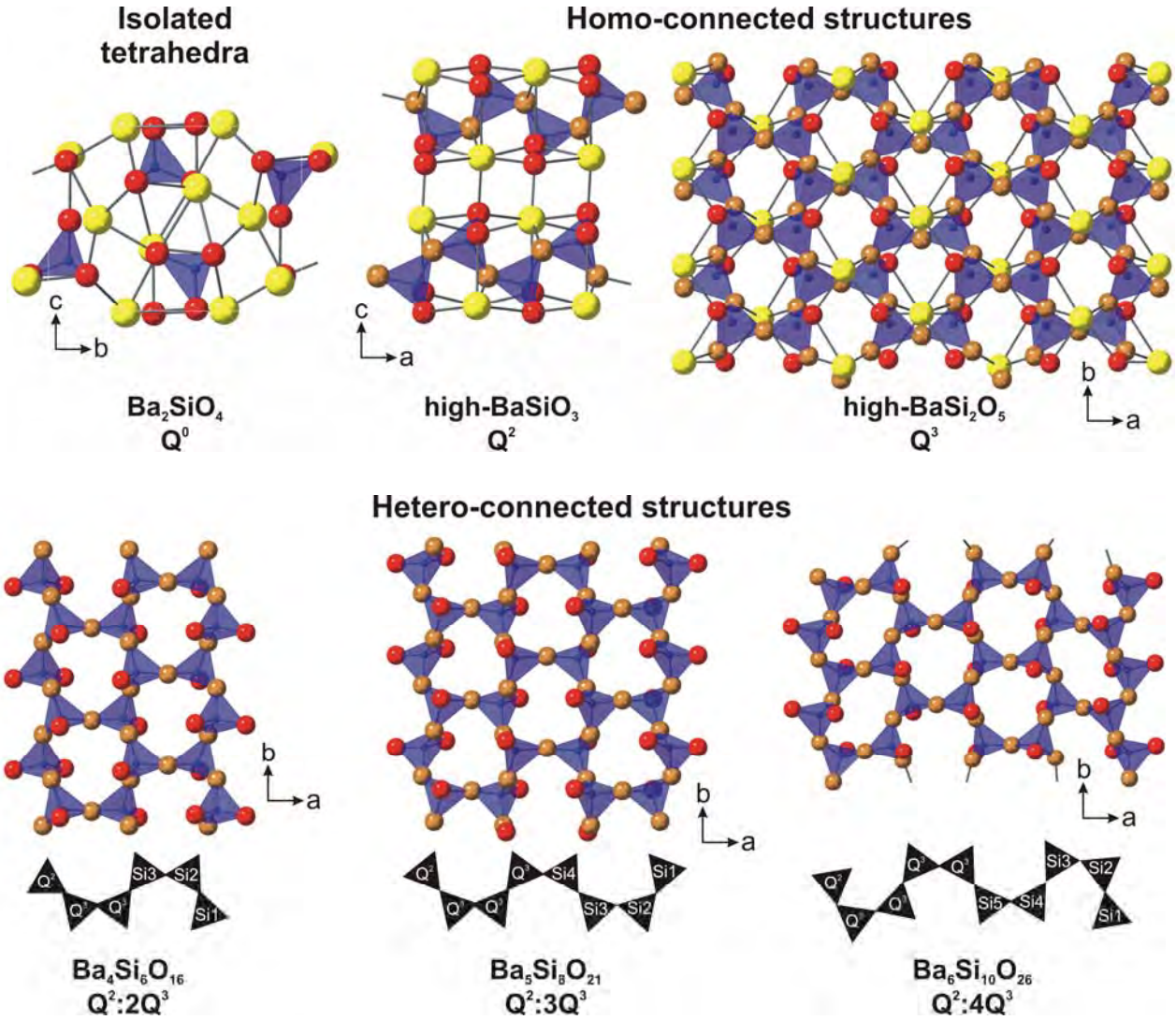

This is the peer-reviewed, final accepted version for American Mineralogist, published by the Mineralogical Society of America.
The published version is subject to change. Cite as Authors (Year) Title. American Mineralogist, in press.
DOI: https://doi.org/10.2138/am-2021-7910. http://www.minsocam.org/

Fig 2

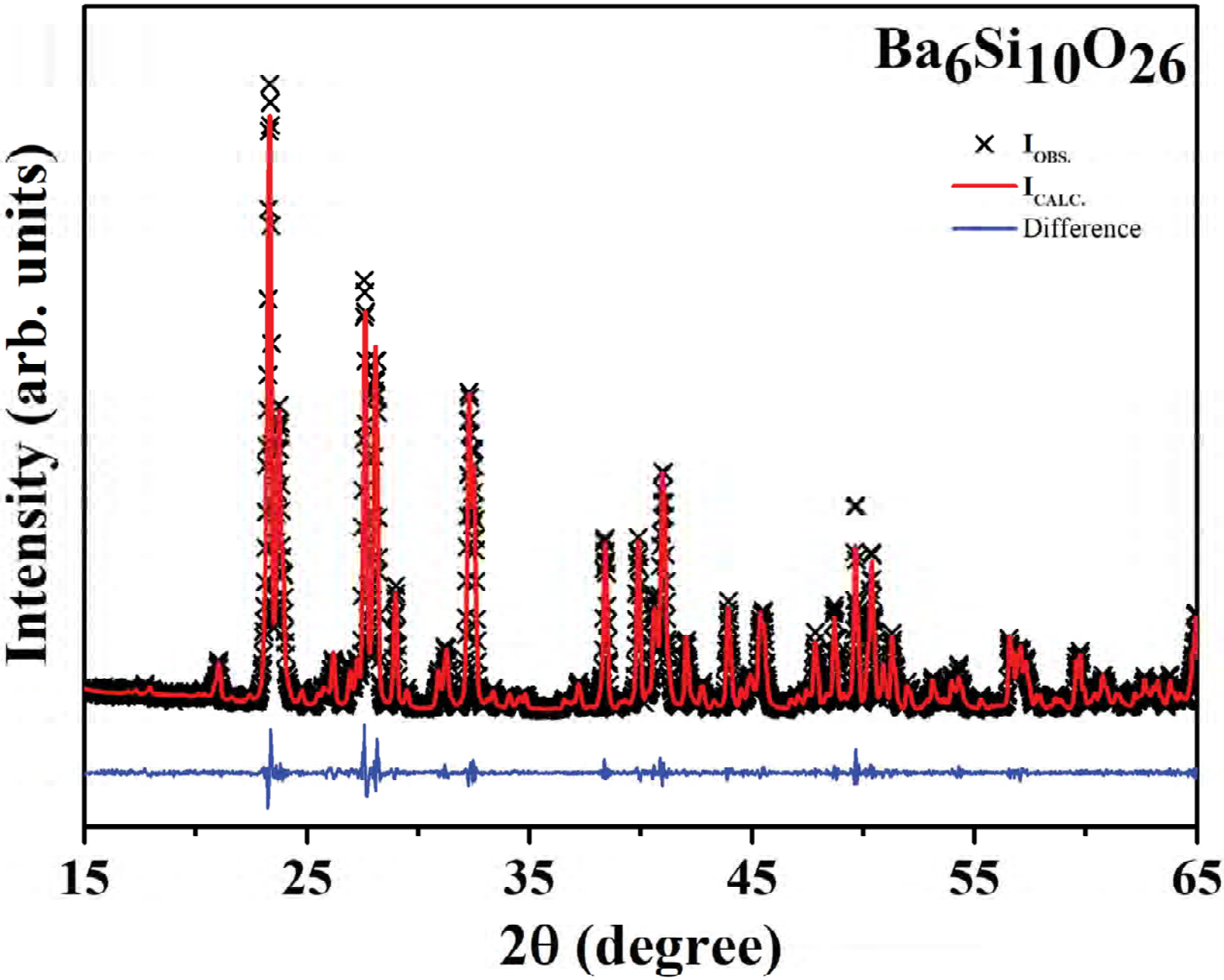

This is the peer-reviewed, final accepted version for American Mineralogist, published by the Mineralogical Society of America.
The published version is subject to change. Cite as Authors (Year) Title. American Mineralogist, in press.
DOI: https://doi.org/10.2138/am-2021-7910. http://www.minsocam.org/

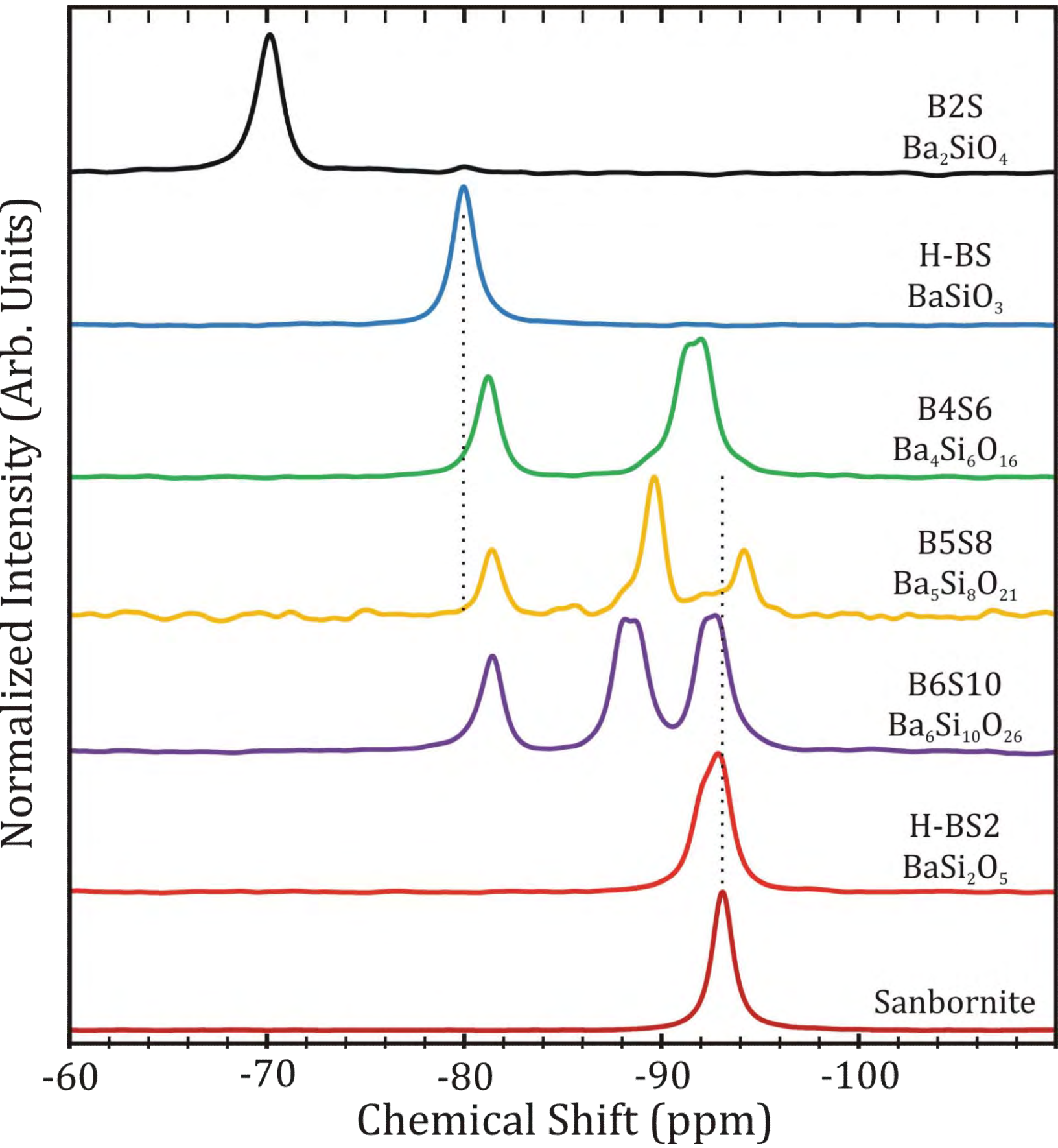

Fig 3 - NMR spectra

This is the peer-reviewed, final accepted version for American Mineralogist, published by the Mineralogical Society of America.
The published version is subject to change. Cite as Authors (Year) Title. American Mineralogist, in press.
DOI: https://doi.org/10.2138/am-2021-7910. http://www.minsocam.org/

FIG 4A

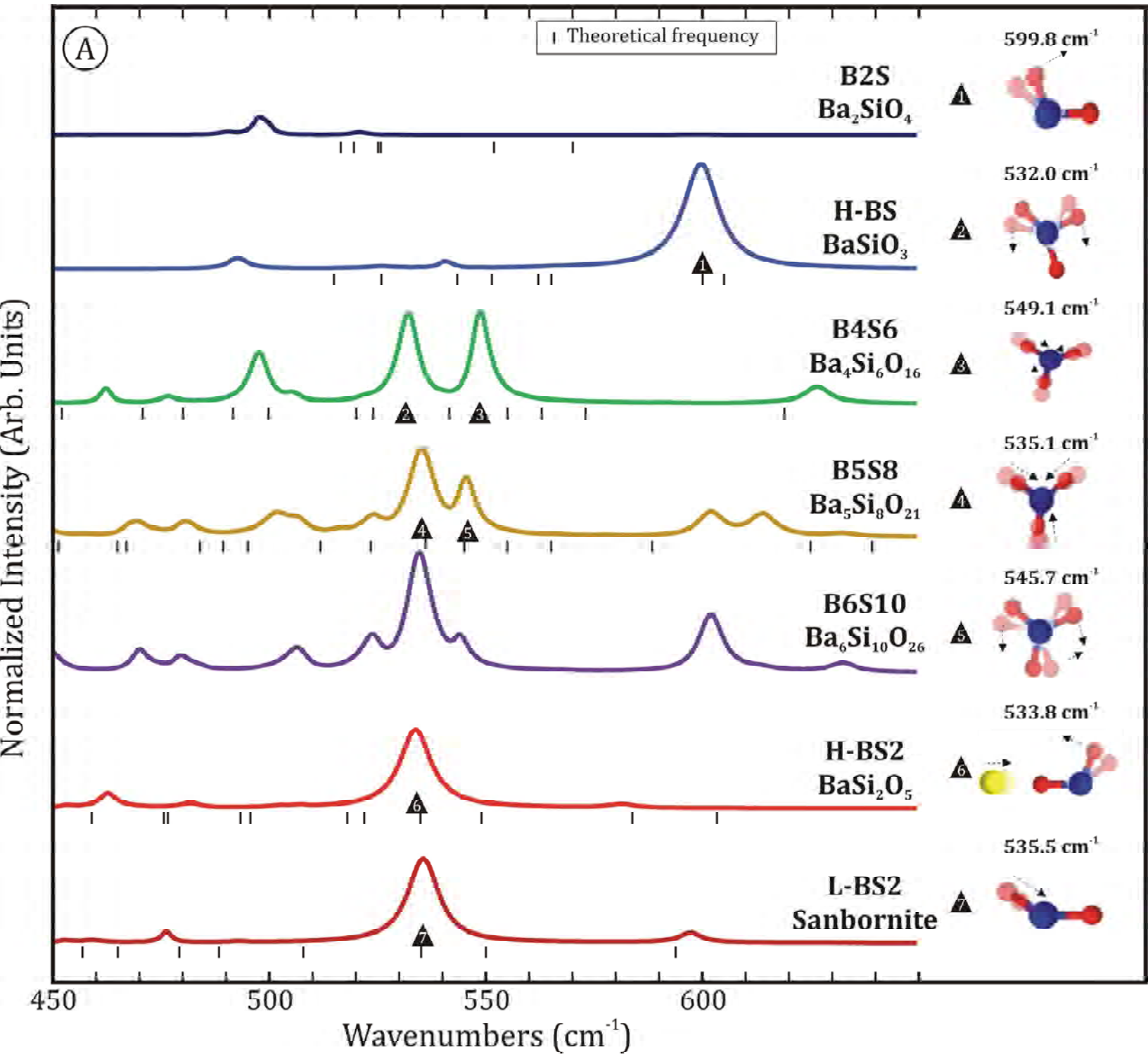

This is the peer-reviewed, final accepted version for American Mineralogist, published by the Mineralogical Society of America.
The published version is subject to change. Cite as Authors (Year) Title. American Mineralogist, in press.
DOI: https://doi.org/10.2138/am-2021-7910. http://www.minsocam.org/

FIG 4B

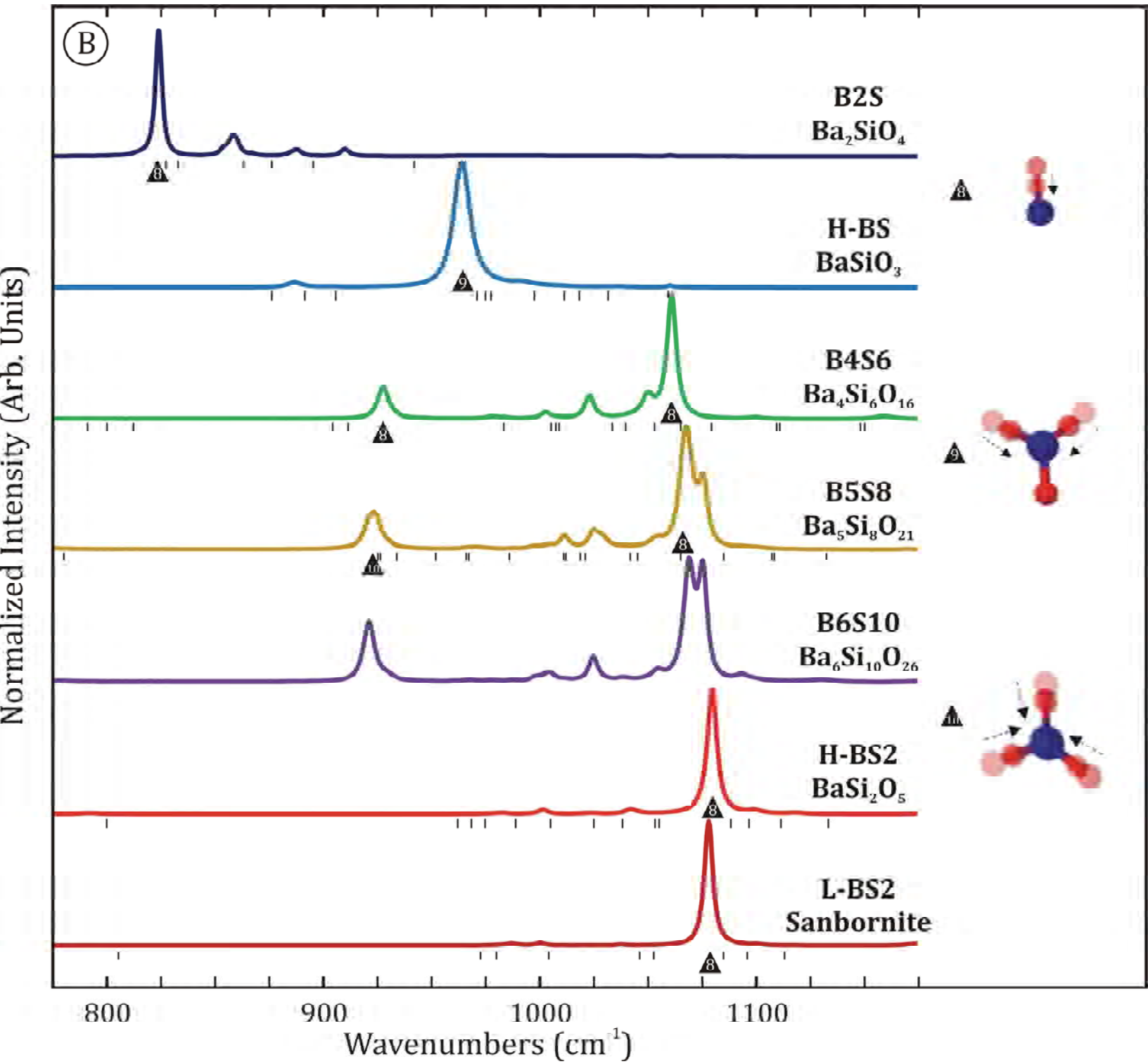

This is the peer-reviewed, final accepted version for American Mineralogist, published by the Mineralogical Society of America.
The published version is subject to change. Cite as Authors (Year) Title. American Mineralogist, in press.
DOI: https://doi.org/10.2138/am-2021-7910. http://www.minsocam.org/

FIG 5

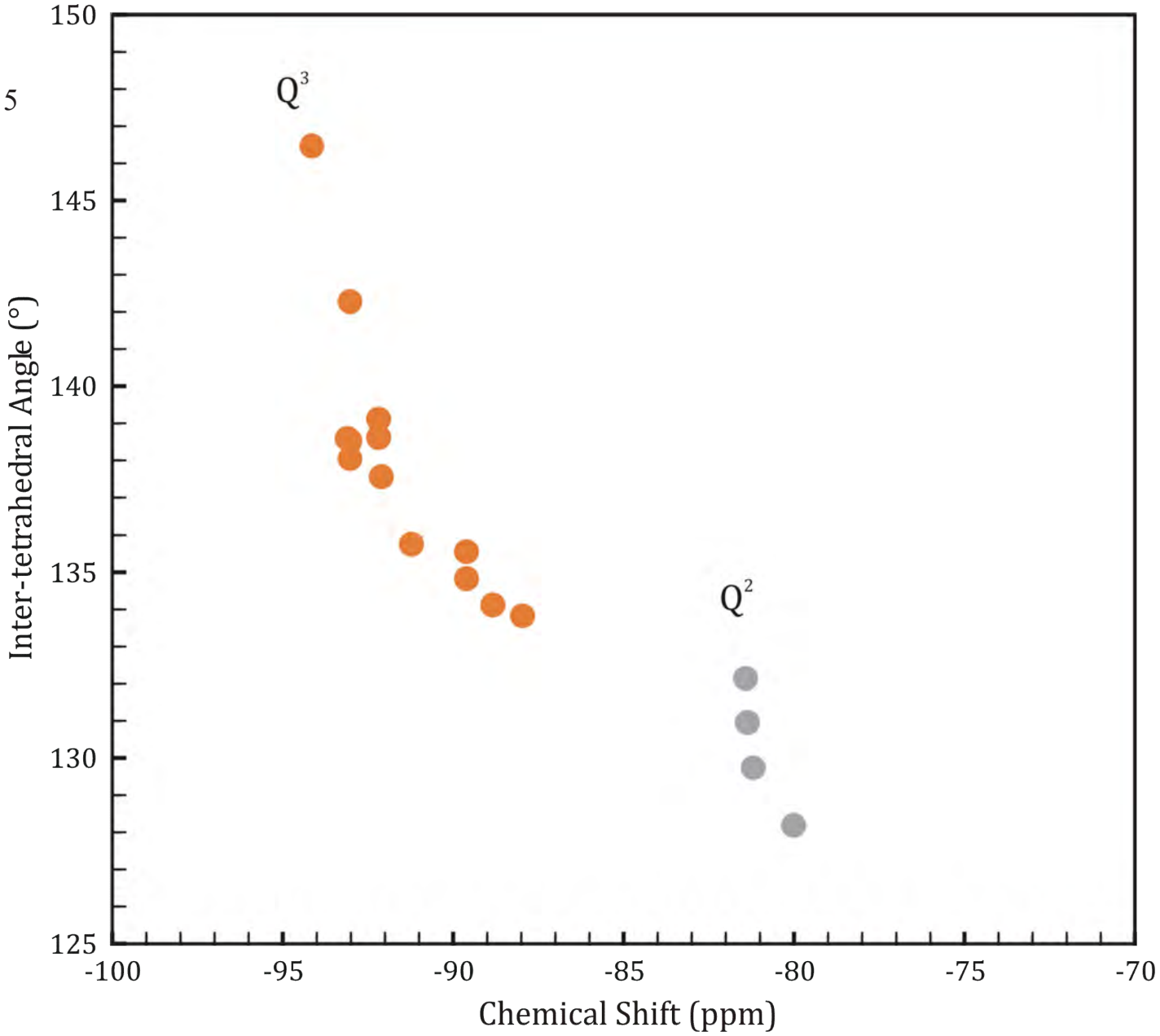

This is the peer-reviewed, final accepted version for American Mineralogist, published by the Mineralogical Society of America.
The published version is subject to change. Cite as Authors (Year) Title. American Mineralogist, in press.
DOI: https://doi.org/10.2138/am-2021-7910. http://www.minsocam.org/

FIG 6

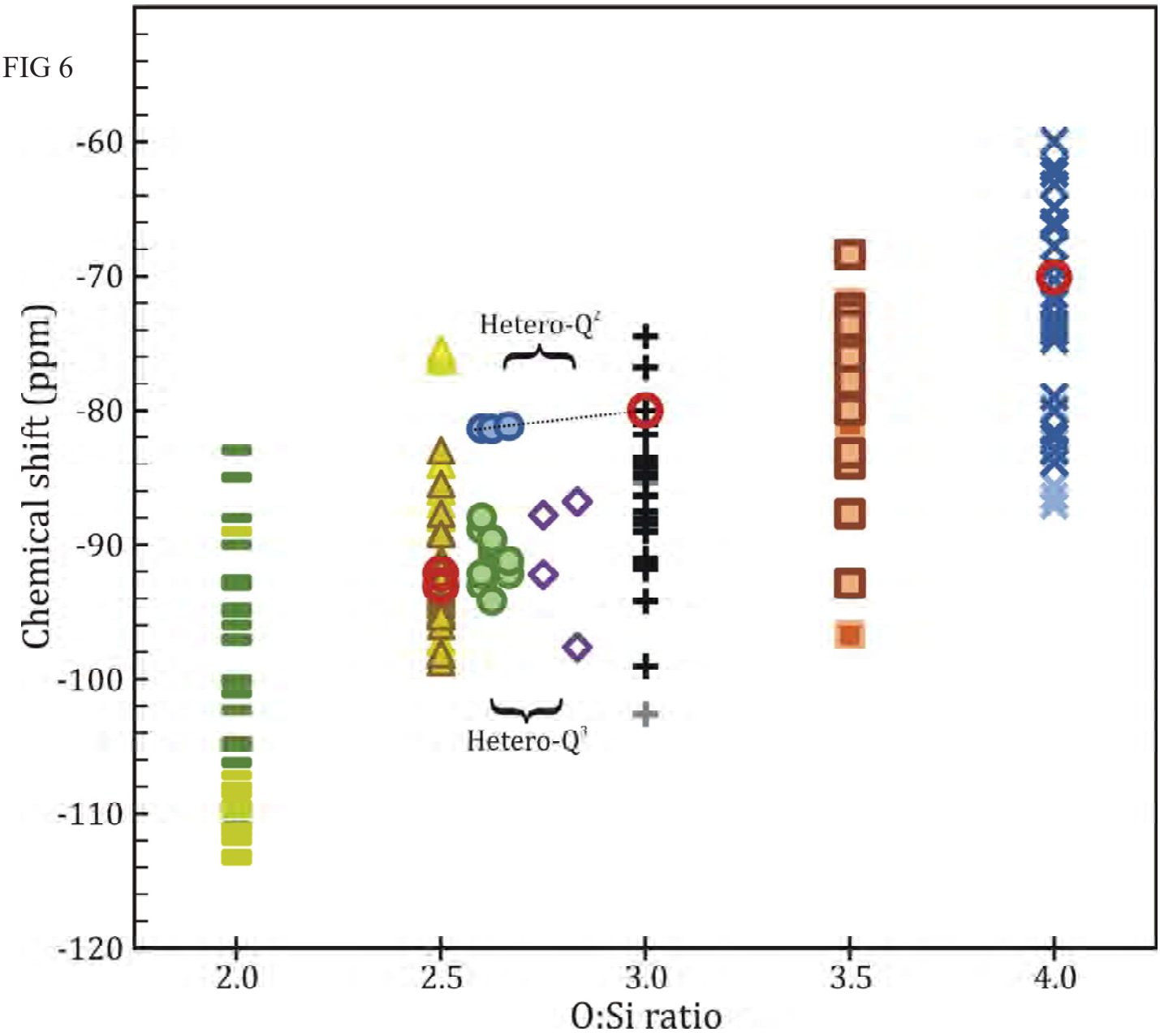

This is the peer-reviewed, final accepted version for American Mineralogist, published by the Mineralogical Society of America.
The published version is subject to change. Cite as Authors (Year) Title. American Mineralogist, in press.
DOI: https://doi.org/10.2138/am-2021-7910. http://www.minsocam.org/

FIG 7

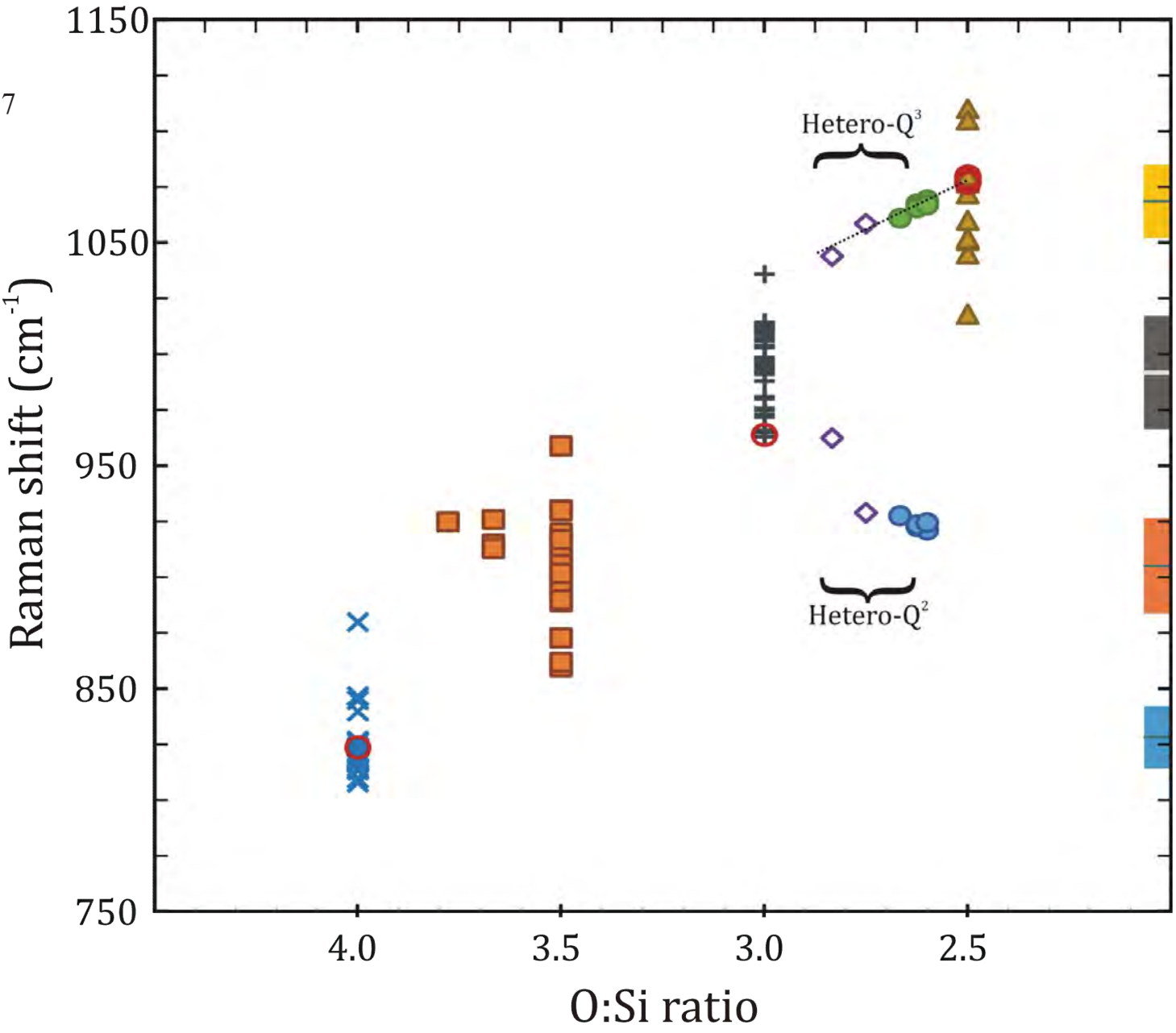

This is the peer-reviewed, final accepted version for American Mineralogist, published by the Mineralogical Society of America.
The published version is subject to change. Cite as Authors (Year) Title. American Mineralogist, in press.
DOI: https://doi.org/10.2138/am-2021-7910. http://www.minsocam.org/

FIG 8